Probing the mechanically stable solid electrolyte interphase and the implications in design strategies

*Yao Gao, and Biao Zhang**

Department of Applied Physics, The Hong Kong Polytechnic University, Kowloon, Hong Kong, China

E-mail: biao.ap.zhang@polyu.edu.hk

Keywords: solid electrolyte interphase, chemical composition, structure, mechanical properties, atomic force microscopy, optimization

The inevitable volume expansion of secondary battery anodes during cycling imposes forces on the solid electrolyte interphase (SEI). The battery performance is closely related to the capability of SEI to maintain intact under the cyclic loading conditions, which basically boils down to the mechanical properties of SEI. The volatile and complex nature of SEI as well as its nanoscale thickness and environmental sensitivity make the interpretation of its mechanical behaviour many roadblocks. Widely varied approaches have been adopted to investigate the mechanical properties of SEI, and diverse opinions have been generated. The lack of consensus at both technical and theoretical levels has hindered the development of effective design strategies to maximize the mechanical stability of SEIs. In this review, we outline the essential and desirable mechanical properties of SEI, the available mechanical characterization methods, and important issues meriting attention for higher test accuracy. We also scrutinize previous attempts to optimize battery performance by tuning SEI mechanical properties, elucidate inconsistencies in these efforts and explore the underlying causes. Finally, we propose a set of research protocols to accelerate the achievement of superior battery cycling performance by improving the mechanical stability of SEI.

1 Introduction

Further improvements in energy density, charging rate, and serviceability at extreme temperatures of secondary batteries all require stable cycling as a premise. The solid electrolyte interphase (SEI) is a thin layer composed of electrolyte reduction products covering the anode surface, which is closely related to the cyclic performance of the battery.[1] The reduction of electrolyte takes place when the lowest unoccupied molecular orbital of the electrolyte is below the Fermi energy of the anode. The formation of SEI consumes not only the salt/solvent of the electrolyte but also the transferred charge (**Figure 1**a and 1b), which leads to a low Coulombic efficiency (CE) in the first cycle.[2] The adverse impact of SEI is reversed after it completely covers the anode surface. An ideal SEI is electronically insulating and ionically conductive, which prevents continuous electrolyte reduction without interfering with ion diffusion.

The enormous volume change of the anode during charge/discharge cycles can greatly challenge the ability of SEI to provide passivation protection for the anode.[3] The capability of SEI to control or adapt to volume variations of the anode is critical to the cycling stability of battery.[4] Degraded cell performance due to the failure of SEI to maintain integrity has been widely observed.[5] In metal-ion batteries, the loose structure of SEI has led to the widespread belief that it ruptures before the active material does.[6] The mechanical analysis of SEI on graphite anode in Li-ion batteries provides theoretical support and application scope for this claim. The stress in graphite particles originates from the diffusion of Li ions, while the stress in SEI stems from the volume expansion of lithiated graphite particles.[4e] At low temperatures or high charge/discharge rates, the high concentration gradient of Li in the graphite particle generates tremendous stress, resulting in the pulverization of the graphite particle.[4d] While for general test conditions, fragmentation and reformation of SEI is the dominant aging mechanism.[4e] Theoretical analysis of Si anodes yields similar conclusions.[4b] Experimentally, breakage-reformation[4c] (Figure 1c1) or cracking delamination[7] of SEI have also been observed by in-situ atomic force microscopy (AFM) characterizations. The continuous fracture-reforming process of SEI consumes the electrolyte and the transported charge, resulting in a decrease in battery capacity. For metal anodes, if the fractured SEI is not repaired in time, the fracture can easily become a location for rapid dendrite growth, which eventually leads to short-circuit failure of battery (Figure 1c2).[8]

The importance of SEI in determining battery performance makes optimizing SEI a very effective method to improve cycling stability.[8c, 9] SEI-related battery failures are usually caused by SEI rupture and the most direct attribute that determines whether an SEI will break is its mechanical properties.[10] However, given the theoretical complexity and experimental

difficulty, systematic analysis of the mechanical behavior of SEI is very rare. Here, we provide an overview of the basic and desirable mechanical properties of SEI, existing mechanical characterization methods, and essential issues to be aware of to improve test accuracy. Since the nanostructure of SEI is closely correlated with the mechanical properties, we categorize the reported SEI structure until now in section 3 after outlining the milestones during SEI development in section 2. The fundamental of the mechanical properties of SEI and the approaches to probe them are discussed in sections 4 and 5, respectively. Considering the predominant role of the AFM-based nanoindentation technique (AFM-NT), we provide a detailed analysis in section 6. Afterward, the efforts to enhance battery stability by modulating the mechanical properties are elaborated in section 7. Meanwhile, we have also identified the inconsistencies in previous attempts and explored the mechanisms behind them in section 8. Lastly, we propose a set of research protocols in section 9 and potential research directions in section 10 to expedite the achievement of superior battery cycling performance by boosting the mechanical stability of SEI.

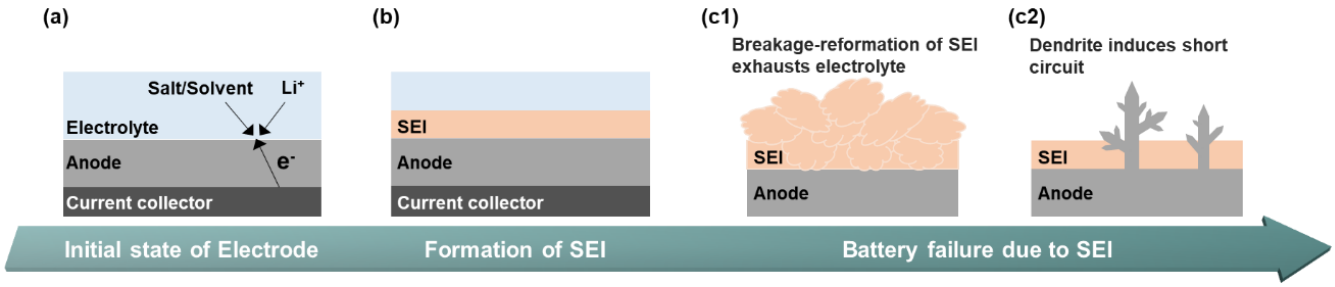

Figure 1. Formation and failure of SEI. The illustration of (a) initial state of electrode, (b) formation and (c) failure of SEI during battery cycling.

2 Milestone timeline

The mechanical investigation of SEI is inseparable from grasping information about its structure. Therefore, the compiled chronology in **Figure 2** contains breakthroughs in the field of SEI structures and mechanical properties.

Advances in SEI structural mechanics pool the efforts of theoretical and experimental scientists and have greatly benefited from the development of testing techniques. The first interphase model between electrode and electrolyte was developed in 1976 to describe the dynamic equilibrium of the hydrated Li oxide film on the surface of Li in Li-H_2O batteries.[11] Three years later, the concept of SEI was articulated in nonaqueous Li batteries to indicate that the layer composed of electrolyte reaction products had the properties of solid electrolyte.[12] The bilayer structure of SEI with a porous outer layer and a dense inner layer was developed in 1982 for the SEI formed in propylene carbonate (PC)-based electrolytes at open circuit potential.[13]

Later in 1986, the compact-stratified layer (CSL) model, consisting of two different homogeneous sub-layers, and the solid-polymer layer (SPL) model with average properties of solid and polymer electrolytes were proposed to describe the properties of SEI.[14] In 1996, a multilayer model of SEI was suggested to reflect the effect of compositional changes of SEI along its thickness direction on electrochemical impedance spectroscopy (EIS) measurements.[15] Shortly thereafter, the "mosaic model" was thought to better describe the heteropoly microphases of SEI, as the thickness of each layer in the multilayer SEI model was too small to be assigned specific material properties.[16] After 2010, the development of characterization techniques has extremely enhanced the fineness and accuracy of the investigation into SEI structures. For example, in 2011, the SEI bilayer structure with a porous organic outer layer and a dense inorganic inner layer was verified by the time-of-flight secondary ion mass spectrometry (ToF-SIMS) isotope experiments.[17] In 2012, the SEI of a composite structure with nanoscale crystallites distributed in an amorphous matrix was experimentally observed.[18] In 2016, a multiphase model of SEI together with its evolution during cycling was derived from various in-situ experiment results.[19] In 2020, a nanomosaic-multilayer model of SEI was built based on the tip-enhanced Raman spectroscopy (TERS) studies of SEI on amorphous Si thin-film anode.[20]

The detailed nanostructure of SEIs unravelled by the advanced techniques facilities the probing of the mechanical properties for understanding the roles of SEIs in battery stability. The probation of the mechanical properties of SEI began at the end of the 20th century and has achieved ground-breaking developments in the last decade. In 1999, the importance of the adhesion of SEI components was emphasized. It was pointed out that the lower the adhesion, the weaker the film-forming ability, and thus more electrolytes were consumed to form a complete and protective SEI.[21] In 2005, a theoretical study showed that an SEI with a shear modulus more than twice that of the metal anode helps to eliminate the electrode surface roughening.[22] The first quantitative measurement occurred in 2011, and concluded that the improvement of the contact stiffness of SEI (measured by nanoindentation (NT)) was the main reason for the electrolyte additives to optimize the battery performance.[23] In 2012, the AFMNT was used to examine the mechanical properties of SEI,[24] and over the following decade, this technique continuously developed and has become the primary tool for exploring the mechanical properties of SEI. Trailblazing work includes the generation of Young's modulus mapping of SEI with the peak force quantitative nanomechanics (PFQNM) mode of AFM;[25] the decoding of obtained force-deformation (*F*-*d*) curves into structural characteristics of SEI;[26] the discussion on the effect of the test environment,[27] surface roughness, indentation depth and

underlying substrate[10a] on testing accuracy; the development of a two-step test methodology to separately obtain elastic and plastic properties of SEI;[10a] and the establishment of the correlation between the maximum elastic deformation energy of SEI and the cycling stability of battery.[10] In addition to the AFM-NT test, a few other test methods have emerged since 2015 to assess the mechanical properties of SEI, such as the electrochemical quartz crystal microbalance coupled dissipation (EQCM-D),[28] the surface force instrumentation (SFA) method,[29] and the AFM-based nanoscale bulge test.[30]

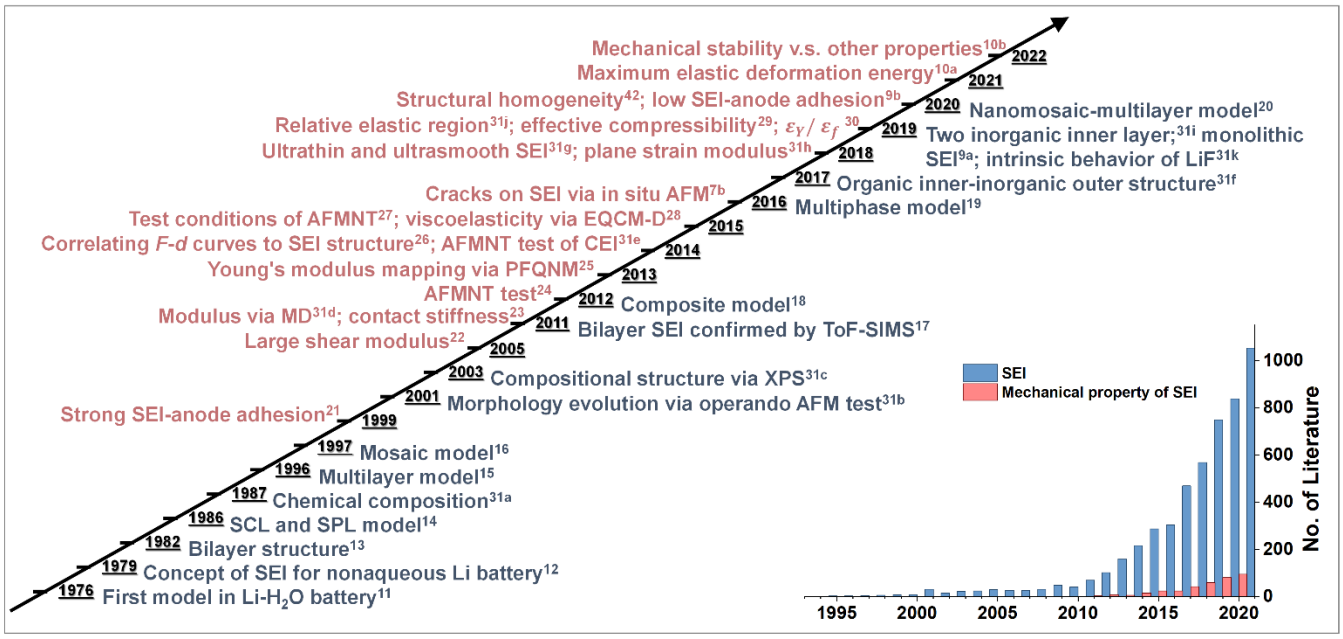

Figure 2. Milestone timeline. Chronology of breakthrough research on SEI structure (dark blue) and mechanical properties (red). The inset at the right bottom corner shows the number of publications as a function of year.[7b, 9-31]

3 Categories of SEI structure

Before discussing the mechanical behaviour of SEI, we need to clarify its different kinds of structures. Otherwise, the correlation between SEI composition and its mechanical properties would be difficult to discern. The chronology in section 2 provides a brief overview of the various structural models of SEI, and this section presents the details. Early investigations of SEI structure were mainly conducted by EIS[14-16] and X-ray photoelectron spectroscopy (XPS) depth profiling.[31c, 32] The development of characterisation tools such as ToF-SIMS,[17, 33] TERS,[20] and cryogenic transmission electron microscopy (Cyro-TEM),[9a, 31j, 34] helps unravelling the SEI structure with a much higher resolution. The structure of SEI determines the functional expression of each constituent in the SEI. A comprehensive understanding of the composition-structure-property relationship of existing SEIs is a prerequisite for the rational design of future SEIs.

In this section, we classify the existing structure models of SEI into three groups based on the distribution of components along the thickness direction. The first group has a certain regularity in the component distribution, including multilayer, bilayer, and gradient SEI models (**Figure 3**(a-c)). The second group has either uniform or randomly distributed components and includes mosaic, composite and monolithic models (Figure 3(d-f)). The third group includes more complex and specific structures, usually a combination or variation of the first two group of models (Figure 3(g-i)).

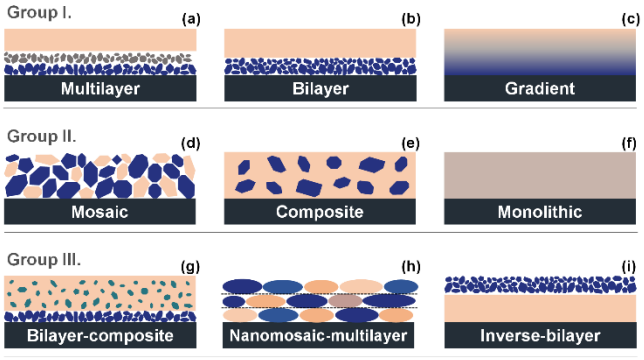

Figure 3. Categories of SEI structure models.

3.1 Regularized composition distribution along thickness direction.

3.1.1 Multilayer SEI.

The multilayer model (Figure 3a) was originally proposed to fit the EIS results.[15, 35] It was later validated by the stepped *F-d* curves obtained from the AFM-NT tests of SEI.[26, 36] In 2019, a combination of various in-situ tests and simulations revealed that the inorganic layer of SEI formed on a silicon wafer anode with native oxides consisted of two sub-layers: the Li_xSiO_y layer and the LiF layer.[31i] However, the additional Li_xSiO_y layer stemmed from the lithiation of SiO_2 and is not representative of multilayer SEIs on other anodes. Attempts in 2018 on electrochemically polished metal electrode surfaces opened the door to artificially construct SEIs with multilayer structures.[31g] By applying different potential steps, ultrasmooth and ultrathin SEIs with alternating inorganic-rich and organic-rich hybrid multilayer structures were produced. In particular, the SEI with an inorganic-organic-inorganic structure realized the coupling of stiffness and elasticity, which greatly optimised the cycling stability of Li metal batteries.[31g]

3.1.2 Bilayer SEI.

Bilayer SEI is one of the most reported structures. The bilayer structure is often described as a dense, protective inorganic-rich inner layer and a porous, electrolyte-permeable organic-rich outer layer (Figure 3b).[9b, 24, 37] This bilayer structure of SEI was confirmed by molecular dynamics (MD) simulations[31d, 38] and various experimental results including chemical analysis

by XPS,[9b, 39] ToF-SIMS,[17, 40], in situ liquid-SIMS,[37c] focused ion beam (FIB) - scanning electron microscope (SEM),[41] cyro-TEM[39b], and mechanical characterization by AFM-NT,[42] EQCM-D,[43] and SFA.[29] There are multiple explanations for the origin of this bilayer SEI. For example, the inorganic-rich inner layer of SEI may be formed from the reduction of the primary oxide layer on the surface of Li anodes or copper current collector,[31d, 43a] or originate from the decomposition of salt/solvent/additive in the electrolyte. The organic-rich SEI outer layer consists mainly of decomposition products of the solvent. That is, the structural stratification of SEI is due to the distinct reduction sequences of different components in the electrolyte.[43a, 43c] It is generally believed that components with higher thermodynamic instability are preferentially reduced.[44] The electrode potential of the anode significantly affects the Gibbs free energy change of the solvent reduction reaction on the anode surface, leading to the experimental observation of the formation of mosaic and bilayer SEI structures at high and low potentials, respectively.[44b] In addition to this, the electric double layer (EDL) has recently been found to play a decisive role in controlling the competitive reduction reactions to form SEI.[37c, 45] Specifically, during the initial charging process, the negatively charged anode surface attracts the solvated Li^+ ions and repel the anions, resulting in the formation of EDL. Only species participating in the cationic solvation shell can be accumulated at the anode surface and be preferentially reduced. Operando liquid-SIMS experiments observe that the cation-anion separation in the EDL leads to the formation of a thin, dense, inorganic-dominated SEI inner layer, which is electrically insulating and Li^+ conductive.[37c] Based on these findings, using the decomposition sequence of different components in the electrolyte to control the structure and performance of SEI becomes an effective and important optimization method, such as polishing or etching away the surface oxide layer,[31g] adding easily decomposable additives or multi-valent cation additives to the electrolyte,[45-46] and using high-concentration electrolytes.[37c] In addition to naturally formed SEI during cycling, bilayer SEI can also be constructed by pre-treating the electrodes, such as immersing Li plates into Deoxo-Fluor solution[47] or using the spray quenching method to generate a LiF rich layer together with lithiophilic Zn nanoparticles on Li surface.[48]

3.1.3 Gradient SEI.

The composition of the gradient SEI varies along the thickness direction but lacks distinct interlayer boundaries (Figure 3c). For example, in the acetamide-Zn $(TFSI)_2$ eutectic electrolyte, the content of ZnF_2 and S/N-rich organics in the SEI formed on Zn anode gradually increased and decreased, respectively, with decreasing distance from the anode surface.[49] The addition of bisfluoroacetamide (BFA) (0.5-2 wt%) to the $LiPF_6$/ethylene carbonate (EC) - dimethyl

carbonate (DMC) solution was also found to form a gradient SEI.[50] Li metal anode in a highly compatible low-polarity solvent, 2-methyl tetrahydrofuran, can generate gradient-structured SEI with a gradual increase in the abundance of inorganic components from the surface to the interior by applying a short initial nucleation modulation procedure.[51] For artificial SEIs (A-SEIs), pre-treating Li surface with poly(ethyleneglycol) diacrylate (PEDGA) - co - vinylene carbonate (VC)/CuF_2/$LiNO_3$/DME solution[52] or FeF_3/$LiNO_3$/DME solution[53] generated either PEGDA-co-VC polymer-based gradient SEI or Fe-based valence gradient SEI.

We find that many reports on the bilayer structure of SEI lack explicit experimental evidence for layering, such as no distinct interlayer boundaries were observed in either the XPS depth profiling results or in the SEM/TEM elemental mapping. It is possible that some gradient SEIs were misclassified as bilayer structures. Whether the interlayer boundaries exist in SEI can seriously affect its mechanical response to anode volume change. Therefore, it is important to provide sufficient experimental data on the delamination phenomenon for the bilayer structure in future studies.

3.2 Uniform/random composition distribution along thickness direction.

The Group II structural models of SEI with ascending rank of orderliness in the thickness direction are mosaic, composite and monolithic.

3.2.1 Mosaic SEI.

The first mosaic model of SEI was proposed to replace the multilayer model in the analysis of EIS results, since each layer of the latter was too thin to impart material properties.[16] The mosaic model nowadays mainly refers to the haphazard accumulation of various components of SEI. This structure is primarily observed in SEIs with inorganic substances as the main components.[54] It is important to note that the mosaic structures (Figure 3d) we delineate here have little or no basal phase. The SEI structure in which the basal phase clearly exists (Figure 3e) is classified as composite SEI.

3.2.2 Composite SEI.

The composite structure of inorganic/organic particles dispersed in an amorphous organic matrix is another common SEI model (Figure 3e). Composite SEIs were chiefly formed in carbonate-based electrolytes and have been reported in Li/Na ion batteries and Li/K metal batteries.[10b, 18-19, 31j, 34a, 55] Recently in the ether-based electrolyte of LiTFSI-DOLDME, the composite structure SEI of LiF and Li_2O nanocrystals embedded in an amorphous polymer matrix was also observed by cyro-TEM.[56] This structure contains a basal phase and an inclusion phase. The basal phase in naturally formed SEIs were generally amorphous organics, and the intercalated particles were predominantly crystalline inorganic salts and sometimes may

contain nanoscale graphite fragments.[18, 34a] The content,[10b] size,[55c] and dispersion homogeneity of the inclusion phase,[34a, 55c] as well as the interfacial strength between the two phases[55b] all impact the mechanical stability of SEI. Composite SEI allows optimization of its various properties by tuning the two constituent phases, thus becoming a popular template structure for A-SEIs. For example, A-SEIs with a composite structure were formed by dispersing Cu_3N nanoparticles in a flexible polymer binder matrix of styrene butadiene rubber (SBR),[55a] or by treating the electrode surface with different chemical reagents (acrylates,[55b] reactive polymer composite precursors[34a]) to create a polymeric network connecting inorganic components of SEI.

3.2.3 Monolithic SEI.

The SPL model proposed in 1987 is the first single-layer SEI model. The SPL model reduced the property of SEI to the average of the solid and polymer electrolytes, which is more like a mathematical approach than a structural model.[14] Only in recent years has it been found that SEIs with a homogeneous single-phase structure (Figure 3f) are formed in electrolytes of 1 M LiFSI/DME-TFEO,[9a] 1 M $LiClO_4$/tetraethylene glycol dimethyl ether (TEGDME),[43b] 1 M $NaBF_4$/diglyme;[31j] 2 M KFSI/triethyl phosphate (TEP),[57] 4 M KFSI/diethylene glycol dimethyl ether (DEGDME),[58] 1 M,[59] 3 M,[60] and 5 M[59] KFSI/DME. Single-phase does not mean that there is only one chemical component of SEI, but that the chemical components that make up SEI cannot be distinguished from each other by current characterization methods, i.e. there are no clear boundaries between different components. This is very beneficial to the mechanical stability of SEI, as which will be detailed in section 7 and 8.

3.3 Other complex structures

The basic SEI models in groups I and II can be extended or combined into more complex models in group III. For example, the SEI formed on graphite in 1 M $LiBF_4$/EC-DMC has an overall composite structure with inorganic particles embedded in the polymer matrix. The inorganic particles were distributed in a layered structure, with the outer layer dominated by the decomposition products of Li_2CO_3 and $LiBF_4$ and the inner layer dominated by LiF.[31c] In 1 M $LiPF_6$/EC-DMC, the SEI formed on the Li metal surface has a bilayer-composite structure (Figure 3g). The inner layer was rich in Li_2O, and the outer layer formed a composite structure with some inorganic materials and most organic substances (Li_2CO_3/$ROCO_2Li$).[61] Based on the fine resolution of the compositional structure by the TERS technique, it was found that the SEI on the anode of the amorphous silicon film in 1 M $LiPF_6$/EC-DEC possessed multiple layers, each of which had a mosaic structure (Figure 3h).[20] In addition, pre-treating the electrode surface can also reverse the composition of the inner and outer layers of traditional bilayer SEIs.

For example, a bilayer SEI composed of an inorganic outer layer (LiF) and an organic inner layer (Spiro-O8-Li) was formed by drop-coating Spiro-O8 on the surface of Li metal anode (Figure 3i).[62]

4 Mechanical properties of SEI

4.1 Basic mechanical properties

Various phrases have been used to describe the mechanical performance of SEI or its components. This does not facilitate comparisons between research efforts and can easily confuse researchers from non-mechanical backgrounds. Therefore, in this section, we summarize the terminologies commonly used to describe the mechanical properties of SEI and elucidate the physical properties corresponding to these terms and the relationships between different properties.

The response of a solid to external forces is generally divided into three stages: elastic deformation, plastic deformation, and fracture. Shape changes due to elastic deformation are fully recoverable upon removing external loads. The scope of elastic deformability is related to parameters of yield strength (σ_Y) and elastic strain limit (ε_Y), which are the upper limit of elastic stress and strain values, respectively (**Figure 4**a). Stress (σ) is the ratio of the internal resisting force (F) of the solid over its cross-sectional area (A). Strain (ε) is the ratio of the change in length (ΔL) to the original length (L_0).[63] The parameters that represent the ease of elastic deformation are modulus and stiffness. Modulus refers to the amount of stress required to achieve a unit of strain, and stiffness describes similar concept but with force and deformation. Modulus is an inherent property of a material, independent of the shape and size of the solid and can be calculated from the linear elastic region of the stress-strain curve (Figure 4a). While, stiffness, and its corresponding phrases of flexibility/compliance, are extensible properties that depend not only on the properties of the material itself, but also on the shape and size of the solid. Different types of moduli correspond to different loading conditions. For example, bulk modulus (K) exists when an object is uniformly loaded in all directions, Young's modulus (E) is for uniaxial compression or tension, while shear modulus (G) is for the case of shear external forces. Given two homogeneous isotropic linear elastic materials, all these moduli have the same relative magnitude assuming they have the same value of Poisson's ratio. Furthermore, hardness in the field of materials and engineering mechanics refers to the resistance to localized plastic deformation caused by mechanical indentation or abrasion. However, in the field of SEI research, hardness often has a similar meaning to stiffness.[63]

When the stress exceeds its yield strength (or when the strain reaches ε_Y), the solid enters the plastic deformation stage. The part of strain beyond ε_Y is irreversible after the external force is

removed. The maximum stress a material can withstand before failure is the ultimate strength (σ_u). Compressive strength and tensile strength are usually the abbreviations of ultimate compressive strength and ultimate tensile strength, which correspond to the maximum stress that the material can stand before breaking in compression or tensile test, respectively. Among these strengths, we think the yield strength is the most critical to SEI. Not only the yield strength corresponds to the elastic limit of SEI, but also it is a material property that does not change with the test method, the sample size, shape, and defects. As a result, the yield strength values measured on different samples using different characterization methods can be directly compared. On the other hand, the compressive and tensile strength values are closely related to the test condition and environment, and usually need to be reported according to specific technical standards. This makes it difficult to obtain these two values of SEI, at least at the current stage.

The maximum strain a material can have before fracture is called the strain at fracture (ε_F), also known as ductility. Ductile material has high deformability, corresponding to the sum of elastic and plastic deformation. The opposite of ductile material is brittle material, which fractures rapidly once it yields, i.e., has particularly little capacity for plastic deformation. The area under the stress-strain curve indicates the deformation energy. For example, the deformation energy within the elastic zone is resilience, and the energy before fracture is toughness, not fracture toughness. This is because fracture toughness does not correspond to energy, but has a specific meaning in materials science that describes the capability of resisting crack propagation under applied stress.[63]

In summary, the parameters describing stress values that SEI can withstand are various strengths: yield strength, compressive strength, tensile strength, etc. The parameters for the degree of deformation that SEI can undergo are elastic strain limit, ductility, and brittleness. Parameters including various moduli, stiffness/hardness and flexibility/compliance represent the ease with which SEI deformation occurs. Resilience and toughness refer to the energies that a material absorbs during deformation. Moreover, there is a very common term, robust, which describes the ability of a system to maintain its functionality and integrity in the face of external disturbances and correlates with no specific mechanical parameters.

4.2 Desirable mechanical properties of SEI

With a clear understanding of basic mechanical properties, we discuss in this section the desired mechanical properties of SEI to maintain its integrity in response to anode volume changes. The effect of homogeneity and thickness is also analysed as they significantly affect the mechanical properties.

4.2.1 Homogeneity

The homogeneity of SEI is divided into two aspects: composition and structure. As we discussed in section 3, there are two forms of compositional inhomogeneity in SEI: along the thickness direction and perpendicular to the thickness direction, in this section we only focus on the latter. The structural inhomogeneity generally refers to fluctuations in SEI thickness or morphological undulations of SEI surface. The homogeneity of SEI has long been recognized as a key factor in determining its stability, whereas inhomogeneities in chemical composition,[20, 64] Young's modulus,[65] and structural morphology[66] are widely observed in naturally grown SEIs. Several findings suggest that interactions between local inhomogeneities (mechanical, electrical, morphological, or chemical) also result in battery failure. For example, inhomogeneity impairs the electronic insulating performance of SEI and may promote dendrite growth at weak sites.[67] Around features with large roughness and small curvature radius, it tends to cause local accumulation of Li and dendrite growth, as well as stress concentration and mechanical failure.[68] Simulations of a quantitative electrochemical-mechanical model based on the finite element method (FEM) showed that increasing the structural homogeneity of SEI was the most effective way to improve its stability when the compositional heterogeneity of SEI was ignored.[31l] The inhomogeneity of SEI partly originates from the initially rough electrode surface, because the reduction reaction of electrolyte is also affected by the electric field distribution on the electrode surface. From this point of view, the creation of smooth electrode surfaces can serve as the first step to improve the uniformity of SEI, especially for metal anodes.[31g]

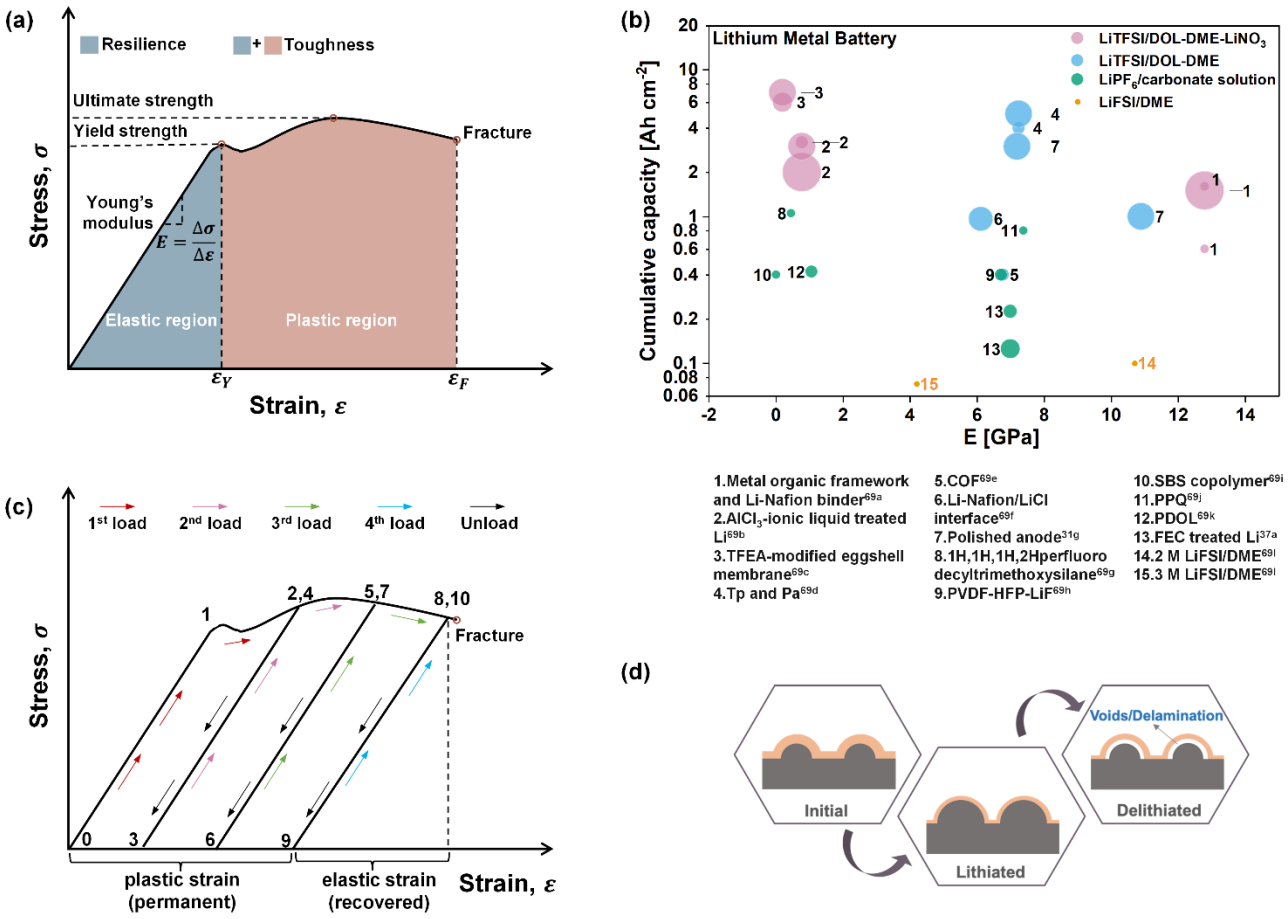

Figure 4. Mechanical properties of SEI. (a) Introduction of basic mechanical properties of SEI with a typical stress-strain curve for elastic-plastic materials. (b) The relationship between cumulative capacity (current density multiplied by the total cycle time) of symmetric Li|Li cells and Young's modulus of SEI.[31g, 37a, 69] (c) Illustration of the consumption of plastic deformability during cyclic loading-unloading process. (d) Plastic deformation of SEI generated during the lithiation process may create voids or delamination between anode and SEI during subsequent delithiation.

4.2.2 Thickness

There is no firm conclusion about the ideal thickness of SEI because theoretical calculations showed that a thicker SEI was beneficial to preventing SEI fracture[70] and reducing the internal stress of anode particles[4e] during cycling. While thinner SEIs can more easily achieve single-phase structures by suppressing the nucleation and growth of crystalline phases in the SEI.[31j] In addition, thinner SEI is more favourable to reducing impedance and promote ion transport. Therefore, adjustment of SEI thickness is always a trade-off, and the optimal thickness may vary from system to system.[70]

4.2.3 Modulus

Large modulus:

The linear elastic mechanical analysis conducted by Monroe and Newman showed that for SEI with Poisson's ratio close to that of polymer materials (for example, polyethylene oxide: 0.33[71]), interfacial roughening was mechanically suppressed when the shear modulus of SEI was about twice that of Li.[22] Their analysis provides a rationale for eliminating dendrite growth by increasing the modulus of SEI. Later 2D FEM simulation results showed that due to the low yield strength of Li (0.73-0.81 MPa[72]), the stress generated by the separator with Young's modulus of 16 GPa would easily cause plastic deformation of Li, resulting in flattening of the anode surface.[73] These theoretical simulations suggested that SEIs with large moduli can enhance the smoothness of metal anodes by generating plastic deformation flows on them.[73b]

A large modulus of SEI is also beneficial for the cycling stability of the insertion electrodes. For the anode with a hollow-core shell structure, the mechanical analysis showed that stiff SEI with larger fracture energy could better withstand the hoop tensile stress generated during lithiation without fracture.[70] The wrinkling and ratcheting behaviour of SEI during battery cycling was investigated using a bilayer model, in which an elastic thin film (SEI) rested on a cyclically deformed elastic-plastic substrate.[74] The results indicated that the mechanical instability of SEI, including wrinkling and ratcheting, can be prevented by introducing an artificial SEI with sufficient stiffness and thickness and/or adding pre-tensile stress to the SEI. The SEI with higher Young's modulus can also improve the mechanical stability of the anode by creating a larger compressive force in the graphite particles.[4e]

Small modulus:

The preference for SEI with a small value of Young's modulus is commonly seen in theoretical analysis or simulation works of Li-ion batteries. Lowering the modulus of SEI significantly reduced the peak tensile hoop stress of SEI on the cylindrical anode.[75] The interfacial jump stress between SEI and the graphite anode in the core-shell structure decreased from 2.9 GPa to 66 MPa when the component of SEI changed from Li_2CO_3 (E=66 GPa, v=0.25) to polypropylene (E=1.1 GPa, v=0.45). To remain intact during cycling, the ultimate strength of SEI should exceed the interfacial jump stress. For the two values of 2.9 GPa and 66 MPa, inorganic salts have difficulty reaching the former, while the latter is achievable for many engineering polymers.[76] A reduction in the occurrence of SEI fracture in the SEI/Si model was also observed when Young's modulus of SEI was decreased.[4b]

Discussion:

Figure 4b summarises the relationship between the cumulative capacity (current density multiplied by total cycle time) of Li|Li symmetrical cells and the Young's modulus of SEI, where cell systems using similar electrolytes are shown in the same colours.[31g, 37a, 69] These

results show no direct correlations between the *E* of SEI and the cumulative capacity. The relationship between the *E* of SEI and the total cycle time at the same current density and capacity density is further compared. Considering that the electrolyte is unlikely to be completely consumed within the reported cycle times, the most likely cause of battery failure is a short circuit induced by dendrite growth. Therefore, the cycle time can reflect the ability of SEI to inhibit dendrite growth. SEI with larger *E* is found to be beneficial in suppressing dendrite growth when cycling at a lower current density (e.g., 0.5 mA cm^{-2}).[69l] As the current density increases, such as when the current density is greater than 5 mA cm^{-2}, the SEI with a large modulus is no longer effective in inhibiting the growth of dendrites.[31g, 69a-c] The possible reason is that the function mechanism of high modulus SEI to inhibit dendrite growth is to plasticize the protrusions of deposited Li, thereby flattening the deposited morphology, but this takes some time to proceed and is more effective when SEI has higher integrity, and the deposited Li is not too coarse. When the current density is high, the nucleation and growth of Li happen very fast, and there is not enough time for plastic deformation to occur. Furthermore, once the SEI is broken, there is also not enough time to form a new SEI to prevent further growth of Li dendrites at the break, eventually leading to short-circuit failure of the battery. Therefore, the high modulus advantage of SEI decreases with increasing current density, while the disadvantage of low deformation ability that usually accompanies the high modulus of SEI is amplified.

In summary, theoretical studies show that SEI with a large modulus can plastically deform and flatten the metal anode surface and relieve the tensile stress field of insertion anode particles by generating large compressive stress. On the other hand, SEI with a small modulus can reduce the risk of SEI fracture by generating lower internal stress when the anode expands. A large modulus increases the attack power of SEI towards the anode, while a small modulus strengthens the defence power of SEI. Combined with experimental results, we find that the realization of these functions of Young's modulus may be affected by some kinetic factors in the actual process. Therefore, the magnitude of the most favourable *E* value for SEI mechanical stability varies for different cycling conditions. Finding the best compromise between these two capabilities of SEI, i.e., offense and defence, or finding ways to achieve a win-win situation is a very important topic in the field of SEI mechanics at this stage. For example, FEM simulations for the Li metal anode found that when Young's modulus of SEI was over 3 GPa, the further increment was not effective in improving the battery's performance.[31l] Another instance is an experimental work constructing a composite SEI film in which ion-conducting ceramic particles were embedded in an ion-insulating polymeric matrix. The special feature of this

composite film is that the top and bottom surfaces of the ceramic particles were not covered by the matrix but were exposed to the electrolyte and can act as ion transport channels. Given the strong adhesive interface between the ceramic particles and the matrix, the ion-insulating polymeric matrix with a low Young's modulus still prevented dendrite growth.[77] The significance of this work is that it takes advantage of the attack power of high modulus ceramic particles and the defence power of low modulus polymer matrix concurrently, demonstrating that smart structure-function design is an important way to effectively optimise the SEI performance.

4.2.4 Elastic strain limit and plasticity

Unlike the ambiguity of the ideal Young's modulus value of SEI, a large elastic strain limit of SEI is always desired for superior cycling performance. This is because the volume change of anode is usually unavoidable, especially for alloy anodes in metal-ion batteries. Once the strain of SEI exceeds its elastic strain limit (ε_Y), it steps into the stage of irreversible plastic deformation (Figure 4c).[31j, 78] Although the plasticity of SEI can compensate for elastic deformation to a certain extent and buffer the occurrence of fracture, its existence may also reduce the cyclic stability. For example, the unrecovered plastic deformation of SEI during delithiation may create porosity or delamination between the SEI and anode (Figure 4d). This will increase the resistance to Li diffusion in subsequent cycles, and the SEI is likely to peel away from the anode once penetrating cracks are formed.[41] Furthermore, for a given sample, the total amount of plastic deformation is fixed. The plastic deformation that happens in each cycle continuously consumes the total plasticity (Figure 4c).[69e] When the plasticity of SEI is depleted, it behaves like a brittle material in the following cycles, which fractures rapidly after yielding.[79] Here we quote from a previous simulation work of SEI on Si anode as a summary of SEI plasticity, i.e., to mitigate SEI failure, local plastic deformation must be effectively suppressed without loss of plasticity itself.[80]

4.2.5 Resilience

In addition to the ambiguity of the required Young's modulus itself, there may be another trade-off between Young's modulus and the elastic strain limit. Because in general, a material with a larger modulus usually has a smaller elastic strain limit.[63b] When it is not clear which parameter is more important, the resilience of SEI (that is, the maximum elastic deformation energy) can be used as a measure of the mechanical stability of SEI.[10, 81] The resilience of SEI reflects the combined effect of E and ε_Y, corresponding to the maximum deformation energy that can be reversibly absorbed and released by the SEI during battery cycling. The evaluation of SEI resilience depends on the analysis of the stress state and the accurate measurement of

basic mechanical properties. For different battery systems, E and ε_Y may have different weights in the expression of resilience.

4.2.6 Toughness/strain at fracture

The resistance of SEI to fracture can be expressed by the total deformation energy before fracture (toughness) or the strain at fracture (ε_F). To evaluate these two parameters, a complete stress-strain curve needs to be constructed, including elastic, plastic, and fracture regions. This is currently difficult to achieve for the SEI case. Some researchers have used the force values at the fracture point of the AFM force-deformation curve to compare the fracture resistance of artificial SEIs.[33a] Although this force value is not a material property and is influenced by many test parameters, it is a big step forward in describing the fracture behaviour of SEI. In addition to toughness and strain at fracture, fracture toughness is another commonly used description of the ability of a material to resist fracture when cracks are already present. However, the determination of fracture toughness requires a more sophisticated experimental design (e.g., pre-crack generation in the SEI) and is currently difficult to implement. We look forward to pioneering works in this direction, as the fracture resistance of SEI is a vital but least studied property.

5 Mechanical test methods of SEI

To date, several methods are available for measuring the mechanical properties of SEI. We summarise the testing capabilities of these methods in Table 1 and plot the proportion of each technique currently utilised in **Figure 5**a. It shows that AFM-NT is by far the most commonly used method. In this section, we describe each of the methods that have been used to characterize the SEI's mechanical properties and discuss in depth the details that need attention in AFM-NT test in the next section.

5.1 AFM-NT test

AFM-NT test can provide in-situ characterization of the formation and growth of SEI using an equipped electrochemical cell. It also enables ex-situ investigation of SEI under specific cycling conditions. AFM can profile a variety of properties of SEI, including surface morphology, roughness, adhesion, conductivity, and so on. Here we focus on its mechanical testing capabilities. The mechanical examination of SEI can be carried out either automatically by recording and analysing the force-distance data at each position during the morphology scanning[19, 25, 37a, 62, 65b, 69k, 69l, 79, 82] or by manually selecting specific positions for indentation tests after the morphology scanning (Figure 5b).[7a, 10, 24, 26-27, 31e, 31g, 31j, 34a, 36-37, 42, 65a, 69h, 81, 83]

The former method relies on the software for automatic analysis, which is simple to operate, but the results obtained are easily impaired by the surface morphology (roughness, hollow or

solid) of the sample. In addition, when the thickness of SEI is not uniform, the influence of underlying substrate (usually the anode) on the test results varies from position to position, which is difficult to precisely eliminate by subsequent processing.[10a, 30] Therefore, the obtained map of mechanical property incorporates interferences from surface topography and substrate, and the resulting inaccuracy increases with the degree of SEI inhomogeneity.

The other method is to perform individual indentation tests at manually selected positions in the previously obtained surface morphology image of the SEI/anode sample (Figure 5b). During location selection, undulating areas can be purposely avoided to minimize the interference of surface roughness with the assessment of contact area in indentation testing. The experimental parameters of the indentation test (e.g., loading rate and applied force) can also be adjusted to evaluate different mechanical properties of SEI. The mechanical analysis of *F-d* curves obtained from AFM-NT has gone through several stages of development: from taking the slop of the *F-d* curve as the contact stiffness of SEI,[23] to generating *E* of SEI by fitting the *F-d* curve to contact models,[24, 65a] to extracting information about the thickness and structure of SEI from the shape of *F-d* curve,[26] to using forces corresponding to the plastic deformation or fracture of SEI to represent the elastic deformability of SEI,[69e] and finally to the successful evaluation of multiple properties of SEI via conducting two serial tests at the same position.[10a] These developments give us the confidence to fully grasp the mechanical behaviour of SEI in the future. The capability of AFM in characterising electrical and magnetic properties also makes it a very promising platform for studying the mechanical-electrochemical coupling effects of batteries.

Table 1. Mechanical characterization methods of SEI.

Method	Parameters	In-situ	Ex-situ	Wet	Dry	Distribution
AFM-NT	modulus, elastic strain limit, thickness	√	√	√	√	√
Membrane bulge	residual stress, modulus, yield strength, inelastic response	-	√	-	√	-
Elastic buckling	modulus	-	√	-	√	√
Compression	modulus, yield stress, plastic hardening	-	√	-	√	-
Nanoindentation	modulus, elastic strain limit	√	√	√	√	√
SFA	thickness, relative compressibility	√	√	√	√	-
EQCM-D	modulus, thickness, viscosity	√	√	√	√	-
Rheometer	modulus, viscosity	-	√	-	√	-
Laser acoustic wave	modulus, density, thickness	√	√	√	√	-

5.2 AFM-based membrane deflection

The AFM-based membrane deflection test is a special case of AFM-NT (Figure 5c). Since the tested sample is a suspended film laid over a holey TEM grid,[84] this test is more suitable for artificial SEI with good film-forming ability. For an example, a single layer chemical vapor deposited graphene (0.33 nm) was first deposited on a TEM grid with a holey Si_3N_4 window to serve as the support layer for the A-SEI. Then the A-SEI samples were deposited over the graphene-TEM grid. Tapping mode AFM topography imaging was first performed to find damage-free films. AFM deflection tests were then conducted at the centre of the suspended membrane.[33a, 33b, 84] Topography scans were carried out after each deflection test to confirm that the tested film did not undergo permanent deformation, and the test was carried out in the elastic range.[33a, 33b] Following a simplified continuum mechanics model for free standing isotropic thin films under central point loading,[85] the effective elastic modulus calculation can be generated:

$$F = \left[\frac{4\pi E}{3(1-\upsilon^2)}\left(\frac{t^3}{R^2}\right)\right]\delta + (\pi T)\delta + \left(\frac{q^3 E t}{R^2}\right)\delta^3 \quad (1)$$

$$q = \frac{1}{1.05-0.15\upsilon-0.16\upsilon^2} \quad (2)$$

where E, υ, t, and R is the effective Young's modulus, the effective Poisson's ratio, thickness and radius of the suspended area of the film, respectively; T is the pre-tension in the film; F and δ is the applied force and film deflection depth, respectively.

At present, the test method ultimately yields Young's modulus of the hybrid A-SEI-graphene structure, rather than Young's modulus of A-SEI alone. Therefore, it is difficult to compare the differences in mechanical properties between A-SEI and natural SEI. However, with the further development of mechanical analysis models, it is expected that the influence of the substrate graphene layer can be eliminated, and the independent mechanical properties of A-SEI can be obtained. Furthermore, the *F-d* curves obtained by this method are also expected to detect the elastic strain limit of A-SEI if the integrity of the substrate graphene film is good and does not fail earlier than A-SEI. The mechanical properties measured by this method reflect the performance of the entire A-SEI in the suspension zone. For example, the obtained Young's modulus is close to the average value of the entire suspended area, and the elastic strain limit response that may be measured in the future is more of the lower limit of the entire suspended area, that is, the earliest place where irreversible deformation may occur. These values happen to correlate well with the actual cycling performance of the battery. In summary, this method is not suitable for natural SEI, but if the influence of the base graphene layer can be eliminated,

coupled with the analysis of elastic strain limit, it will be a very suitable means to characterize the mechanical properties of A-SEIs.

5.3 Membrane bulge by pressure chamber

The membrane bulge test is another method used to characterize the mechanical properties of freestanding films.[86] This method differs from the method described in section 5.2. The external load causing the membrane deformation is not a point force exerted by the AFM probe, but a lateral pressure exerted by the gas in the pressure chamber. In this method, the pressure applied to the membrane is controlled by argon gas in the bottom chamber of the cell with a resolution of 70 Pa and the AFM is used to monitor the lateral deformation of the membrane at different pressures.[30] The mechanical model used in this test is as follows:

$$q = \frac{2\sigma_0 t}{a^2} w_0 + \frac{4Et}{3a^4(1-\upsilon^2)} w_0^3 \quad (3)$$

where q is the pressure, t, $2a$, σ_0, w_0 is the thickness, the suspended width, the residual stress and the maximum deflection of the film, respectively. During the test, the suspended length of film is larger than six times of $2a$ and the deformation of film is pure elastic. The point at which the measured pressure-deflection relationship begins to deviate from **Equation 3**, is considered to correspond to the elastic deformation limit of the membrane.[30]

When apply this method to mechanically characterize SEI, a thin layer of Li was first deposited on a free standing PDMS film by physical vapor deposition and then was fully converted to SEI by reacting with the electrolyte (Figure 5d).[30] To determine the solely mechanical properties of SEI from the pressure-deflection curve of the SEI-PDMS hybrid structure, membrane bulge test was carried out on bare PDMS films first to determine its stretch stiffness, which was then subtracted from the combined stiffness. This method moves a great step forward to provide averaged quantitative information on the residual stress, plane-strain elastic modulus, yield strength, and inelastic response of SEI and A-SEIs, and provides a direction for generating free-standing SEI films. One issue is that the SEI used in the bulge test was converted from Li film at the open circuit voltage. Both the thickness and uniformity of SEI were highly dependent on the initial Li film. Therefore, it is worth considering whether the SEI formed in this way is representative of the SEI naturally formed during cycling. Furthermore, this method is currently difficult to obtain the special distribution of the mechanical properties of SEI.

5.4 Elastic buckling

The modulus of SEI can also be derived from the elastic buckling test of the hard film-soft substrate samples. The basic mechanism is that compressive strain in rigid film (SEI) constrained on a relatively compliant substrate (PDMS) induces buckling at characteristic

wavelengths to minimize the total potential energy. The unknown mechanical properties of the rigid film can then be evaluated based on the following expression

$$E_f = \frac{3\left(1-\upsilon_f^2\right)E_s}{1-\upsilon_s^2}\left(\frac{d}{2\pi h}\right)^3 \quad (4)$$

Where E_f, ν_f and h are the Young's modulus, Poisson's ratio and thickness of the hard film, respectively; E_s and ν_s are the Young's modulus and Poisson's ratio of the substrate, respectively; d is the characteristic wavelength. [31h, 87]

In the experiment setup, a layer of Li was thermally evaporated onto PDMS substrate and transformed to SEI through the reaction with room-temperature ionic liquid (RTIL). The formation of SEI generated equibiaxial compressive strain and formed wrinkles on the PDMS substrate. The plane-strain modulus of the SEI could be derived from the characteristic buckling wavelength (Figure 5e).[31h] Similar to the uncertainties discussed in the membrane bulge test, the representativeness of the SEI formed in this method remains questionable. Furthermore, it is uncertain whether the generation of compressive strain is a common phenomenon during SEI formation. That is, this test method is selective in terms of samples that can be tested. When the electrolyte system, the mechanical property, or the thickness of the SEI are varied, there is a probability that no wrinkles will be observed.

5.5 Compression

The mechanical properties of nanorods with SEI-related materials Li_2O and Li_2CO_3 were evaluated by compression tests performed with an electrochemical mechanical device (EMD) inside the environmental transmission electron microscopy (ETEM).[88] Initially, a short CNT was welded to the AFM tip by electron beam-induced carbon deposition. Then, the CNT reacted with Li in a CO_2 atmosphere to form Li_2O/Li_2CO_3 nanorod in the sample chamber of the ETEM. The compression test was realized by moving the piezoelectric tube of the holder toward the AFM tip (Figure 5f). The displacement of the AFM tip (Δx) and the change in nanorod length (ΔL) were read out from the TEM images. The force applied in the compression test is calculated as:

$$F = k \cdot \Delta x \quad (5)$$

where k is the spring constant of the AFM cantilever. Then the force (F) - deformation (ΔL) relationship is generated for the nanorod. Finite element simulations were conducted based on the geometrical dimensions determined from the TEM images and the real loading conditions. The mechanical properties of the sample, such as Young's modulus, yield stress and plastic hardening, were determined by systematically adjusting the simulation parameters to match the experimentally obtained force-deformation curve.[88]

This method can provide the complete topographic change of the sample during loading and can obtain various mechanical parameters of the sample by combining with finite element simulation. However, the simulation work required to produce a good fit to the experimental results is enormous and when multiple parameters are involved in the fit, the uniqueness of the fit is difficult to guarantee. When only one angle was photographed for the same test, the determination of specimen geometry may introduce errors. Moreover, this method is also difficult to be applied to real SEIs.

5.6 Nanoindentation

The nanoindentation test is a widely used method for determining the hardness and Young's modulus of materials. The commonly used nanoindentation test is to press a specifically shaped indenter into the sample with vertical pressure. The indenter is sufficiently hard and is equipped with force and displacement sensors (Figure 5g). During the test, control the load to change continuously and measure the indentation depth in real time. Samples for the nanoindentation test need to have smooth and parallel top and bottom surfaces. The Young's modulus (*E*) and hardness (*H*) of tested sample can be obtained following the equations below:

$$E = (1 - \upsilon^2)\left(E_r - \frac{1-\upsilon_i^2}{E_i}\right)^{-1} \tag{6}$$

$$E_r = \frac{\sqrt{\pi}}{2} \cdot \frac{S}{\sqrt{A}} \tag{7}$$

$$S = \frac{dP}{dh} \tag{8}$$

where υ is the Poisson's ratio of tested sample, E_r is the reduced modulus, E_i and υ_i are the Young's modulus and Poisson's ratio of the indenter, *S* is the stiffness, *P* is the load and *h* is the indentation depth. *A* is the contact area and is usually determined by the geometry of the indenter and the depth of contact. When defining hardness as the mean pressure the material will support under load, the hardness *H* is computed from

$$H = \frac{P_{max}}{A} \tag{9}$$

where P_{max} is the maximum load, and *A* is the projected area of contact at peak load.[89]

Compared to AFM-NT, the radius of the indenter adopted in conventional nanoindentation tests is much larger. Nanoindentation testing is usually positioned using an optical microscope and therefore has a lower resolution than AFM scanning positioning. Nanoindentation test is better suited for the mechanical characterisation of large-scale samples, such as A-SEIs or thin-film electrodes, which can be sized specifically to meet the testing requirements.[55a, 69c, 90]

5.7 EQCM-D

The electrochemical quartz crystal microbalance with dissipation monitoring (EQCM-D) can obtain time-resolved quantitative information on various gravitational and mechanical properties of the working electrodes.[28, 43a, 43b, 91] In the setup of EQCM-D (Figure 5h), a quartz crystal plate (resonator) oscillates under an applied AC voltage to generate acoustic shear waves. The acoustic waves then penetrate the thin electrode layer that is rigidly adhered to the quartz crystal. Rigid adhesion means no slip occurs at the interface. The multi-harmonic EQCM-D has two output characteristics: the resonant frequency (*f*) normalized by the overtone scale (*n*), *f/n*, and the dissipation factor, *D=W/f*, defined as the ratio of the full width at half maximum of the resonant peak (*W*) to resonant frequency.

The formation of SEI on the electrode causes changes in the frequency and dissipation of the quartz crystal. The conditions of $\Delta f \neq 0$ and $\Delta D = 0$ indicate that the formed SEI is thin, hard, non-porous, and has a flat outer surface. At this point, a simple relationship between Δf and the mass of SEI (Δm) is given by the Sauerbrey equation:

$$\Delta m = -C \cdot \frac{\Delta f}{n} \tag{10}$$

$$C = \frac{\sqrt{\mu_q \cdot \rho_q}}{2{f_0}^2} \tag{11}$$

where *C* is the mass sensitivity constant, μ_q and ρ_q are the elastic shear modulus and density, respectively, for the thin quartz crystal plate.[92] But when $\Delta f/n$ depends on *n* and $\Delta D \neq 0$, the formed SEI may have the hydrodynamic behaviour of porous solids or the viscoelastic behaviour of soft coatings. Distinguishing the two conditions requires a series of additional EQCM-D measurements.[91a, 92] There are many hydrodynamic or viscoelastic models available to analyse experimentally obtained $\Delta f/n$ and ΔD.[93] Having some advanced knowledge of SEI features through other characterization techniques can help to select a suitable fitting model. For example, the Voigt model is widely used when considering SEI as a soft viscoelastic coating. It relates the measured *f* and *D* as a function of *n*, to the thickness, density, shear elasticity, shear viscosity of SEI.[94] There are some assumptions when using the Voigt model: such as that the film is laterally homogeneous and that the solution viscosity does not contribute to the measured Δf . In addition, it is often needed to estimate density values for SEI.[28]

The EQCM-D method can provide non-invasive in-situ measurements on multiple properties of SEI, including mass, thickness, shear elasticity and share viscosity. Compared with other test methods, EQCM-D has the outstanding advantage of distinguishing properties at different thicknesses of SEI. However, the disadvantage of this method is that the properties it provides

are averaged over the entire surface. It is also difficult to determine whether all these observed changes in frequency and dissipation are induced by the SEI. The choice of analysis model and the fit between the model and the real SEI features also greatly affect the accuracy of the results.

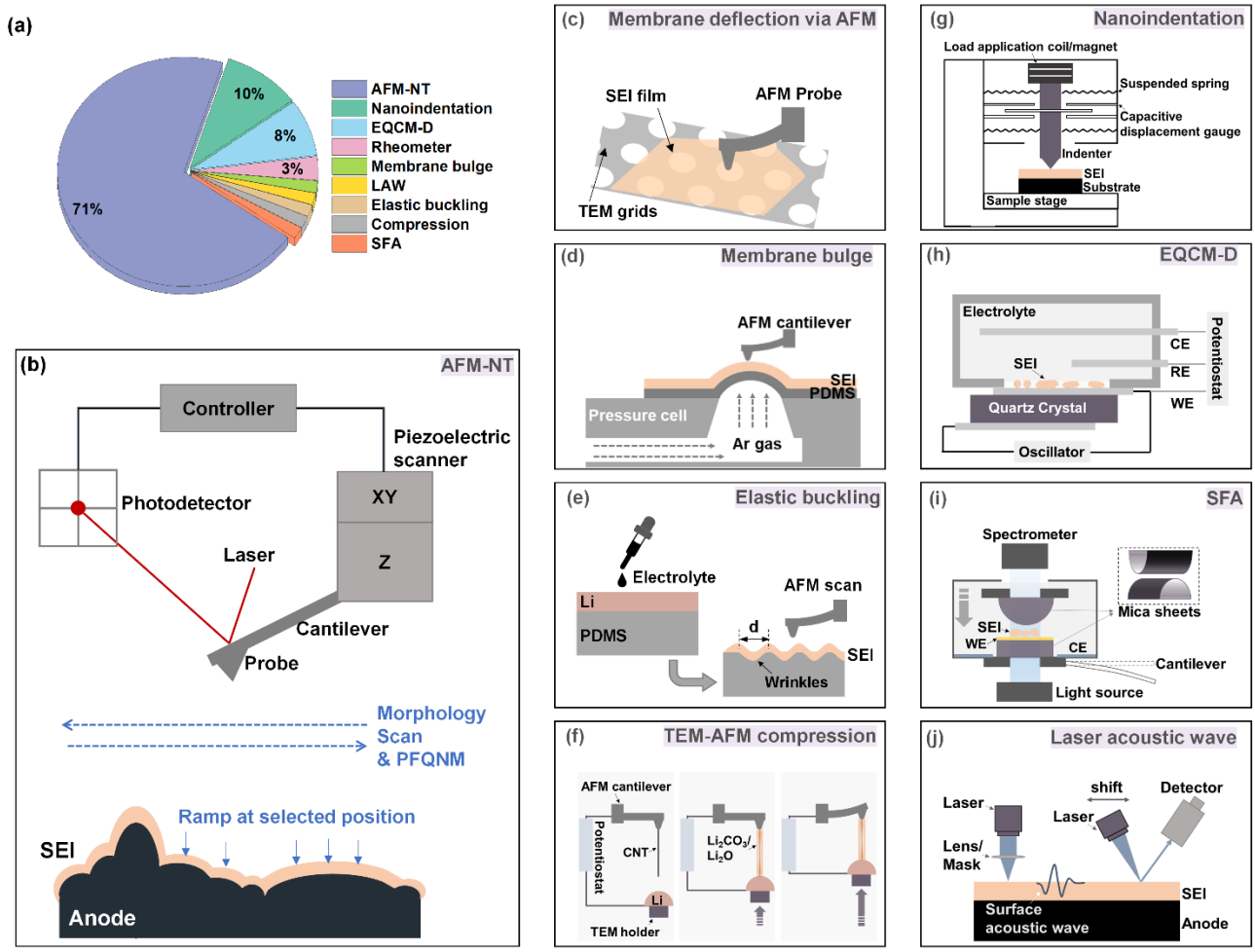

Figure 5. Techniques for mechanical characterization of SEI. (a) Percentages of different methods for mechanical testing of SEI. Illustration of operating principles for (b) AFM-NT test, (c) AFM-based membrane deflection test, (d) membrane bulge test by pressure chamber, (e) elastic buckling test, (f) compression test by combination of TEM and AFM, (g) nanoindentation test, (h) EQCM-D test, (i) surface force apparatus test and (j) laser acoustic wave method.

5.8 Surface force apparatus

The SFA method allows for the evaluation of the thickness and relative compressibility of the SEI. In the SFA setup, two curved silica or mica discs are arranged in a crossed cylindrical geometry (Figure 5i). During the test, white light is guided through these discs. When the discs are close together, the mirrors on the discs form an interferometer and constructive and destructive interference of discrete wavelengths of white light results in so-called fringes of

equal chromatic order (FECO). The change in distance between the two discs can be derived from the position changes of the FECO fringe with a resolution of sub-Å.[95] One of the mica sheets is held in place by a cantilever spring, and the force on this mica sheet can be monitored by recording the deflection of the cantilever. To characterize the SEI using SFA, the electrode material is coated on one of the mica sheets.[29] After or during the formation of SEI, the distance between two micas is manually controlled and the corresponding force is recorded. Using this method, the initial thickness, and the thickness in the fully compressed state of SEI can be obtained. Furthermore, the force-displacement curve during the compression process can also be generated. In the reported case, the compression test of SEI was performed in the electrolyte, which would involve the electrolyte-SEI interactions.[29] The extraction of mechanical properties of SEI from the force-displacement curve requires many assumptions and the analysis process can be complex. However, the force-displacement curve can still provide some useful qualitative information about the variation of the mechanical properties of SEI along its thickness direction.

5.9 Laser acoustic wave (LAW)

In the setup of the LAW test, short laser pulses are used to generate surface acoustic waves. Surface acoustic waves are elastic vibrations which then propagates along the sample surface (Figure 5j). The dispersion of surface acoustic waves is very sensitive to surface conditions. By fitting the obtained dispersion curve to appropriate models, multiple properties of the surface layer can be obtained.[96] To increase the fitting accuracy, the number of parameters that need to be fitted should be as small as possible. For example, to extract Young's modulus value of SEI from the dispersion curve, values for the mechanical properties of the anode, the thickness and density of the SEI are better to be provided based on other independent techniques.[96a] But the tricky part is that density values for SEI are still difficult to obtain accurately. The mechanical properties generated by the LAW method are also averaged over the entire SEI.

5.10 Rheometer

The mechanical property of polymeric artificial SEI layers can be characterized by the frequency-dependent oscillatory shear measurement via a rheometer. In the experiment operation, a strain of 1% was adopted for different superpositions of time and temperature to obtain the rheology data at a wider frequency range. By analysing the recorded stress-strain data, the elastic and viscoelastic behaviour of the polymer layer can be identified. The high and low frequency regimes correspond to the elastic and viscous behaviour of the material, respectively. In short, if the storage modulus of a material is larger than its loss modulus, it

exhibits elastic solid-like behaviour.[97] Currently, this method is limited to polymeric artificial SEIs and can only provide averaged values for the whole tested sample.

5.11 Other methods

Several techniques have been used to qualitatively evaluate the mechanical properties of SEI. Dry collision of active material particles with and without A-SEI was performed in a three-dimensional mixer to qualitatively evaluate the mechanical strength of A-SEI. The integrity of the particles after collision reflects the high mechanical strength of A-SEI. No flaking was observed, indicating that the A-SEI was firmly attached to the anode surface.[98] In addition, the ability of the A-SEI to remain intact after a puncture test with an AFM probe at a certain force value was also used to qualitatively evaluate the property of SEI.[69d]

6 AFM-NT test

6.1 Analysis of the *F-d* curve

Compared to other approaches, AFM-NT captures the broadest range of mechanical information, is suitable for various test environments, and is the most likely method to become the standard SEI mechanical test in the future. In this section, we describe in detail how to accurately evaluate the mechanical properties of SEI by AFM-NT testing. So far, the mechanical parameters of SEI that can be obtained by analyzing the *F-d* curve mainly include Young's modulus, thickness, elastic strain limit and maximum elastic deformation energy.

6.1.1 Evaluation of Young's modulus

A common method to generate the value of *E* is to fit the selected part of the *F-d* curve to a contact model. There are several different contact models, each targeting a particular contact behavior. The most basic and classical one is the Hertz (or Hertzian) model, which describes the non-adhesive elastic contact behavior between a sphere and a sample with a flat surface.[65a, 82c] The *F-d* relationship in the Hertz model is represented by the following equation:

$$F = \frac{4}{3} E_r \sqrt{R d^3} \quad (12),$$

where *R* is the radius of the sphere (AFM tip) and E_r is the reduced modulus expressed as:

$$E_r = \left(\frac{1-v_{tip}^2}{E_{tip}} + \frac{1-v_{sample}^2}{E_{sample}} \right)^{-1} \quad (13).$$

E_{tip} and v_{tip} are the Young's modulus and Poisson's ratio of the AFM probe, respectively. E_{sample} and v_{sample} are the Young's modulus and Poisson's ratio of the tested sample, respectively. v_{sample} is hard to measure and is usually assumed to have a value between 0.3 and 0.5. [24-26, 31e, 31g, 34a, 65a, 82c, 99] With known value of *R*, the experimentally obtained *F-d* curve was fitted to **Equation 12** to obtain the value of E_r. Then the values of E_{tip}, v_{tip} and v_{sample} are substituted into **Equation 13** to derive the value of E_{sample}. Hertz model describes the most

basic contact behavior, and when test situation involves more interfering parameters, Hertz model is modified into different forms to incorporate these variables. For example, Sneddon model [24, 26, 31e, 83a, 99]and Bilodeau model[27, 100] are developed for the conical indenter and the four-sided pyramid indenter, respectively, Johnson–Kendall–Roberts (JKR) model[35] [83b, 101] and Derjaguin–Muller–Toporov (DMT) model[36] [19, 25, 31j, 34a, 37a, 65b, 69k, 82b] are developed considering the adhesive force between the indenter and the tested sample. All these mentioned models are limited to pure elastic deformation and when plastic deformation is involved, more complex theory models are required.[102]

Two representative *F-d* curves are provided in **Figure 6**a and 6b. Three different parts of the *F-d* curve have been used to evaluate E_r: (1) the early region of the loading curve (segment AB in Figure 6a and 6b);[7a, 24, 26-27, 31e, 31g, 31j, 36-37, 42, 69h, 83a, 83e] [66b](2) the upper region of the loading curve (segment BC in Figure 6a);[65a] (3) the upper region of the unloading curve (segment CD in Figure 6a).[10, 34a, 81, 83b-d] The percentage of each analysis approach is provided in Figure 6c. Although fitting segment AB currently dominates, we believe that fitting CD segment has higher accuracy based on the following considerations. The early loading stage of *F-d* curve is easily disturbed by surface contaminants, the collapse of porous structures, slip/stacking of particles, and incomplete contact due to surface roughness, and cannot truly reflect the elastic behavior of SEI. The unloading segment of CD in Figure 6a is less disturbed by the sample morphology and fully reflects the elastic behavior of material. However, if the SEI is cracked or pressed too deeply during loading (Figure 6b), the unloading curve cannot accurately reflect the mechanical properties of SEI.

The AFM-NT method currently has difficulty in defining the mechanical properties of each layer in the multilayer SEI. A "scraping" method has been used to remove the outer SEI layer and then characterize the mechanical properties of the inner SEI layer.[82b] Although the division of layers in SEI depends more on the magnitude of the scratching force, it is the most feasible method at present. Another common approach is to use different intervals of the stepped loading *F-d* curve to assess the Young's modulus of each layer in the SEI.[24, 31e, 37a] An uncertainty in this method is that given the very small thickness of each layer in the multilayer SEI, each segment of the split *F-d* curve still reflects the combined mechanical response of multiple layers. We expect better theoretical treatments to guide experimental tests in the future to achieve an accurate description of the mechanical properties of bilayer/multilayer SEIs.

6.1.2 Evaluation of thickness

The "scratch method" conducted by AFM has been broadly used to determine the thickness of SEI. After the SEI was morphologically scanned by AFM, an area of the SEI was selected, and

then the AFM was operated in the contact mode to scratch the surface with a force of certain value (20 nN,[9b] 500 nN,[25] 3 μN[9b], 9 μN[65b]). The thickness of SEI was generated by analysing the scratched and unscratched scanlines (Figure 6d).[27, 65b, 66b, 69d, 69l, 82a] A large uncertainty of this method is that it assumes that the SEI can be completely removed during the scrape process. The reality is that the extent of SEI removal is highly dependent on the force applied and the number of scrapes.[42] It is extremely arduous to find the critical force value for removing only the SEI and not the anode, especially for the SEI with a dense inorganic inner layer. Another uncertainty is that the bottom and top lines used to determine the thickness of SEI do not originate from the same location. This may cause large errors when the scratched area is small, or the inhomogeneity of the anode surface and SEI thickness is huge.

The *F-d* curve obtained from AFM-NT test is also widely used to evaluate the thickness of SEI. The SEI thickness corresponds to the indentation depth from the start of the elastic region to the end of the plastic region (section AE in Figure 6b).[7a, 24, 31e, 31g, 31j, 83a] The loading segment of *F-d* curve was also used to calculate the thickness of each layer in the bilayer/multilayer SEI.[26, 37a] The risk is that this method will underestimate the thickness of SEI if the SEI layer is not pierced by the AFM probe but only compressed. Furthermore, this method will overestimate the thickness of SEI if the substrate beneath the SEI layer is simultaneously displaced downward during AFM compression. Using this method to determine the thickness of each layer of a multilayer SEI heightens this uncertainty even more. Another important category for determining SEI thickness is from various microscopy images, including Cyro-TEM,[31j, 81, 83c, 101, 103] SEM,[47, 96a] and optical images[83b]. Issues to consider when using these methods are whether the magnification and resolution of the images are sufficiently high and the possible effects of electron radiation on SEI. The thickness of SEI can also be generated from the ToF-SIMS,[33c, 40] EQCM-D,[91b] dynamic thermomechanical analysis,[97b] and the SFA methods[29] (Figure 6e). We summarize the SEI thickness values evaluated from different techniques in Figure 6f.[9b, 10a, 26-27, 29, 31e, 31g, 31j, 39a, 40, 42, 65b, 66b, 69l, 81-82, 83a, 83c, 91b, 101, 103-104] We note there could be large differences in the thickness determined by the *F-d* curve and Cyro-TEM, and usually the value obtained in the former is larger. In addition to the intrinsic differences of tested systems, the difference in mean values may also be influenced by the lower resolution of the *F-d* curves. In future AFM-NT tests, more attention should be paid to the number of data points for a single *F-d* curve and the setting of the maximum loading force to obtain adequate test accuracy. Multiple techniques are also recommended to assess the thickness of the SEI, as its value is important in mechanical analysis.

6.1.3 Evaluation of elastic strain limit

The ability of SEI to undergo reversible elastic deformation can be described by its elastic strain limit, ε_Y. The determination of ε_Y involves plastic mechanics, is more complicated than the assessment of Young's modulus and thickness and is therefore rarely reported.[10] For non-adhesive contact with a spherical probe indenting a flat surface, adopting the von Mises's shear strain-energy criterion or the Tresca's maximum shear stress criterion, when the sample's Poisson's ratio is assumed to be 0.3, and nonlinear elasticity is ignored, its elastic strain limit can be calculated by the following equation[10a]:

$$\varepsilon_Y = \frac{1}{1.6\pi E_{sample}} \left(\frac{6 F_Y E_r^2}{R^2} \right)^{\frac{1}{3}} \quad (14),$$

where F_Y is the external force corresponding to the yielding of indented sample (force at point B in Figure 6b), or the end of elastic deformation. Plastic yielding is a concept widely used in elastoplastic materials but rarely investigated for SEI. The mechanisms of yielding and following plastic deformation are very complicated and generally different for different kinds of materials. Based on studies on existing materials, some preliminary conclusions can be drawn about the yielding and plastic deformation behavior of SEI. For example, the SEI dominated by inorganic salts is expected to have weak plastic deformation ability. For SEIs with composite structures in which inorganic salts are entrapped in an organic matrix phase, its plastic yielding may be more dependent on the softer organic matrix phase.[105] More research work is needed to elucidate the plastic behavior of SEI and its impact on battery cycling performance.

Besides the elastic strain limit, several other parameters, such as the relative elastic region,[31j] the effective compressibility,[29] the yielding force,[69e] and the puncture resist capability[69d] have been adopted to describe the limit of SEI to deform or to withstand external forces. Compared to the material property ε_Y, other parameters are dependent to some extent on sample size or loading conditions, making direct comparisons between different studies difficult.

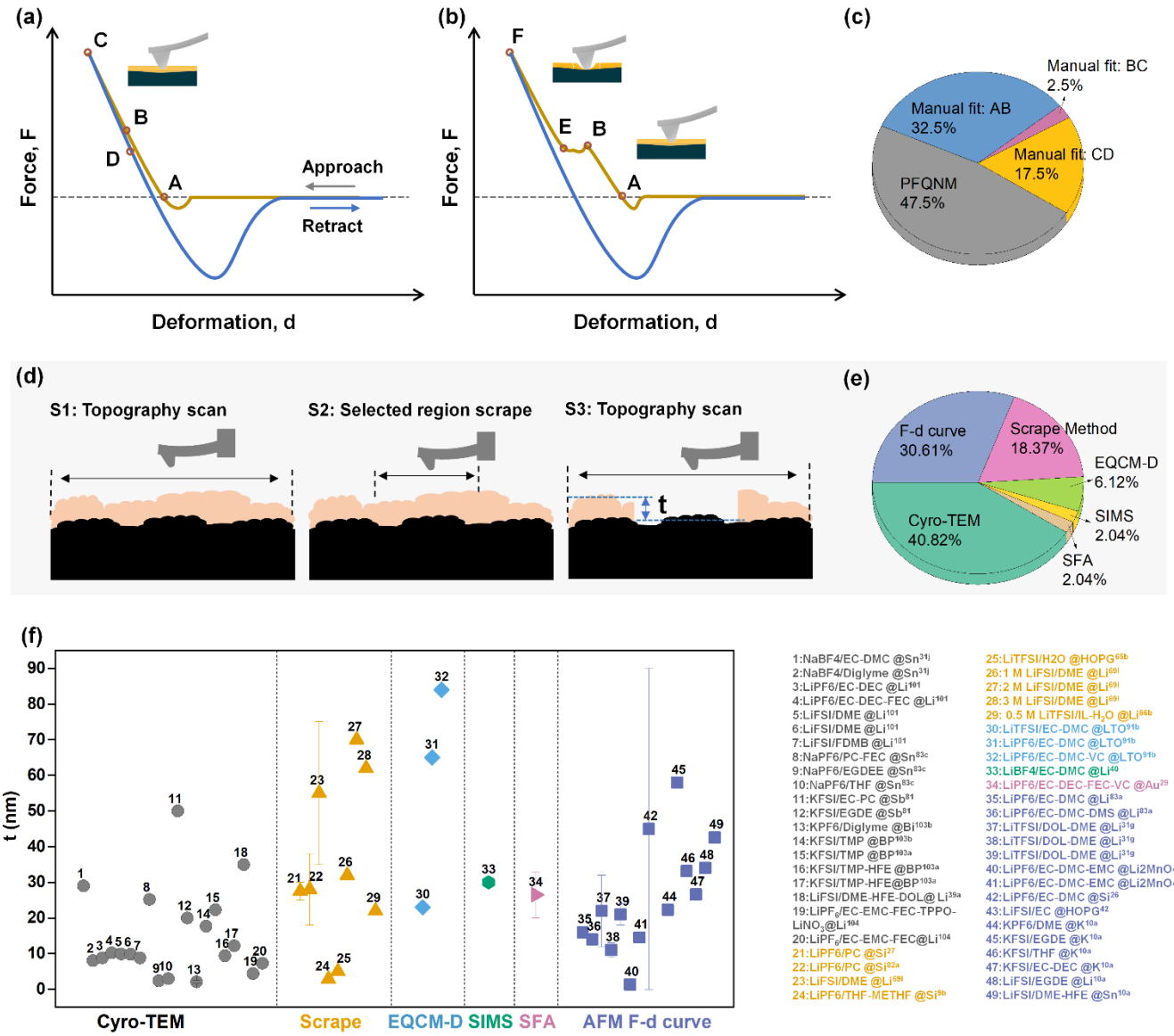

Figure 6. AFM-NT test. Representative force-deformation curves obtained from AFM-NT test (a) without and (b) with yielding/fracture of SEI. (c) Percentages of different analysis methods of the force-deformation curve. (d) Illustration of the "scratch method" used to determine SEI thickness. (e) Percentages of different methods to evaluate the thickness of SEI. (f) Summary of SEI thickness values obtained from different methods.

6.1.4 Evaluation of maximum elastic deformation energy

As we mentioned earlier, sometimes it is hard to decide whether Young's modulus or elastic strain limit plays a more important role in deciding the mechanical performance of SEI, the maximum elastic deformation energy (U) is proved to be a better indicator of the mechanical stability of SEI in various metal and metal-ion batteries.[10, 81, 83c, 83d, 103a] U can reflect the combined effect of E and ε_Y. The magnitude of U corresponds to the area under the force-displacement curve up to the elastic limit:

$$U = \int_0^{d_c} F d(d) \quad (15).$$

The computation of U is flexible when E and ε_Y of SEI are known. For different battery systems, the SEI may experience different stress conditions and the force F will be expressed as different functions of the deformation d.

6.2 Notes on the AFM-NT test

It is found that even in similar electrode-electrolyte systems, the measured Young's modulus values for SEI from AFM-NT test span a very large range. By carefully analysing the test details of each set of data, we believe that the large degree of data dispersion may stem from the following several factors.

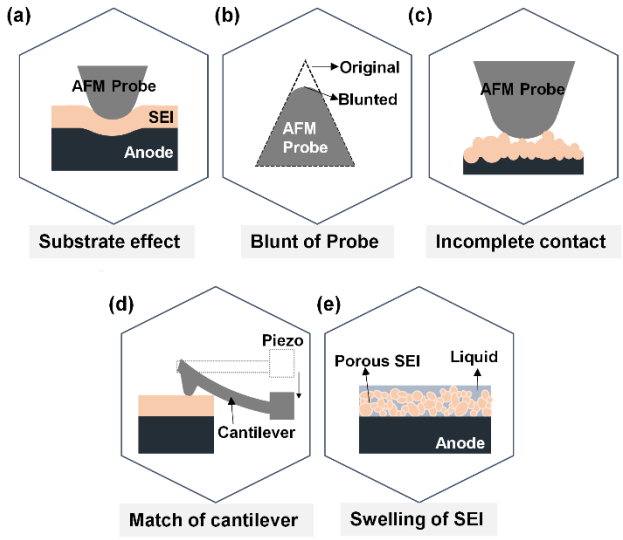

Figure 7. Important issues meriting attention for improving the test accuracy of AFM-NT method: (a) correct for substrate effect, (b) calibrate AFM probe radius before and after each test, (c) ramp at smooth area, (d) select AFM cantilevers with appropriate spring constant; (e) conduct mechanical tests at both dry and wet conditions.

6.2.1 Substrate effect

Similar to the phenomenon of multi-layer SEI interfering with each other during testing, the small thickness of SEI makes the *F-d* curve easily incorporate the mechanical response of the underlying substrate (anode plate) (**Figure 7**a).[10a, 55a, 65a, 106] However, the interference of substrate has been ignored in most experimental works. Finite element simulations of soft films on hard substrates showed that ignoring the substrate effect led to an overestimation of Young's modulus of SEI. The degree of overestimation in E of SEI increases as the ratio between the indentation depth (d) and the SEI thickness (t) increases. The degree of overestimation also increases as the ratio between Young's modulus of the substrate (E_s) and Young's modulus of the SEI increases.[10a, 106b] Even when d/t = 0.05, ignoring the substrate effect leads to a 50%

overestimation of E when E/E_s = 0.014 and a 30% overestimation when E/E_s = 0.57.[10a] The thick-soft and thin-hard SEIs observed in the experiments may stem from the enhanced substrate effect when the SEI thickness is reduced.[106b] Therefore, to improve the accuracy of the test, the influence of substrate cannot be ignored when processing the *F-d* data obtained by AFM-NT. A solution has now been proposed. Using the two-step AFM-NT approach, values of the apparent Young's modulus, thickness, and indentation depth for each test position of SEI were evaluated and then substituted into a recast equation for the reduced modulus to eliminate the interference of substrate on the E evaluation of SEI.[10a]

6.2.2 Blunting of AFM probe

Blunting of the AFM probe is another factor that is easily overlooked when performing AFM-NT test. The initial radius (2–10 nm)[24, 26-27, 31e, 31g, 31j] of the AFM probe cannot be retained all the time and becomes blunt easily during scanning (Figure 7b).[102, 107] Ignoring the increase of AFM probe radius underestimates the contact area between the probe and SEI during the indentation test and therefore overestimates the Young's modulus of SEI. More stable but larger probe radii (eg, 2.5 μm and 3.4 μm)[27, 65a] can be obtained with special spherical probes. The larger radius of these probes makes them less prone to wear, but more susceptible to interference from surface roughness. As shown in Figure 7c, during the indentation test, complete contact is hard to achieve between a rough surface and the probe, leading to an overestimation of the actual contact area and an underestimation of the E value of SEI.[27] In addition, due to the large indenter radius, the elastic response of SEI is averaged over a large area, which attenuates the degree of heterogeneity of SEI. Furthermore, conventional AFM probes with sharp initial radii are more suitable for morphological scanning than specialized spherical probes due to their high resolution. For mechanical testing, accuracy can be greatly improved by calibrating the AFM probe radius with a standard sample before and after each test. In general, AFM probes tend to stabilize after a certain level of wear.[102, 107a] The frequency of the AFM probe radius calibration can be gradually reduced as appropriate. However, it should be noted that the blunting pattern of the probe is easily influenced by probe type, sample type and test parameters, so frequent calibration is important for accurate mechanical analysis with unfamiliar probes.

6.2.3 Spring constant of the AFM cantilever

The spring constant is a fundamental factor to consider when selecting an AFM probe. The spring constant of AFM cantilever used in the experiments ranged from ~2-5 N/m, [31g, 79, 83b] to 20-50 N/m,[10, 31j, 81, 83c, 83d] and to 200 N/m.[82j] The larger the spring constant, the stiffer the AFM cantilever will be. To ensure accurate testing, the spring constant of the AFM cantilever should match the E of SEI being tested. For example, soft cantilevers are difficult to press into

hard samples as most of the deformation is carried by cantilever bending (Figure 7d). Although a stiff cantilever can easily indent a soft sample, the resolution of obtained *F-d* curve will be greatly reduced. In general, when the *F-d* curve obtained from the test sample has a similar slope to the *F-d* curve obtained from the sapphire calibration sample, the cantilever used should be changed to a cantilever with a larger spring constant.

6.2.4 Indentation rate

Ramp rate is a parameter that can be manually controlled during indentation test. A wide range of ramp rates are reported in the literature, from 50 nm s^{-1} to 1 μm s^{-1}.[7a, 24, 27, 31e, 31g, 31j, 83b] The effect of loading rate on mechanical properties is different for elastoplastic and viscoelastic materials.[108] The former is insensitive to the indentation rate, while the modulus of the latter is highly dependent on the indentation rate. If the SEI is viscoelastic, which is common for polymeric materials, the comparison of experimental results at different indentation rates can lead to large inconsistencies. Viscoelastic materials have both elastic and viscous elements. Elasticity corresponds to stretching along crystallographic planes in ordered solids, whereas viscosity is mainly due to the diffusion of atoms or molecules in amorphous materials.[109] The viscoelastic behavior of SEI can be investigated by indentation tests over a wide range of ramp rates, which may correlate with the rate capability of batteries.

6.2.5 Dry or wet test environment

The porous structure of SEI (or the outer layer of SEI) has been verified by various experimental methods, including in-situ AFM,[31b] EIS,[110] and Cyro-TEM.[101] Due to the high capacity of this porous structure to store liquids, SEI exhibits different mechanical behaviours under wet and dry conditions (Figure 7e). Most ex-situ AFM-NT tests of SEI adopted dry electrode plates after cleaning with solvents. The porous layer of SEI may shrink and harden during drying, resulting in a rise in Young's modulus. When tested in the liquid environment, the thickness of SEI increases due to the swelling effect[101] and exhibits mechanical behaviour similar to liquid/solid composites.[110b] The naturally formed SEIs tested in liquid environments generate modulus values of 3 to 62 MPa[25] and 0.5 to 10 MPa[27], both in the lower region of the total reported values (Table 2). Furthermore, a decrease in modulus was also observed when an A-SEI was immersed in the electrolyte compared to the dry state.[97a] For a comprehensive understanding of the mechanical and structural information of SEI, it is best to perform mechanical testing of SEI in both in-situ liquid and ex-situ dry conditions.

6.2.6 The dynamic nature of SEI

In addition to the influence of test conditions, the dynamic nature of SEI can also induce large discrepancy in the measured mechanical properties. The anode type,[111] formation voltage,[19,

[32b, 82a, 112] stabilization time,[82j] scan rate,[18] charging current density,[4b, 113] lithiation/delithiation state,[28, 111b, 114] temperature,[115] cycle number,[19-20, 66a] and different positions of electrode[7b] all affect the property of SEI.

Anode type:

The type of anode, whether in metal batteries (K vs. Li)[111a] or metal-ion batteries (graphite vs. AlSb)[111b], was found to affect the dominating component of SEI, even in similar electrolytes.

Stabilization time:

In both LiTFSI/DME and LiFSI/DME electrolytes, the modulus of SEI formed at open circuit potential was found to decrease with increasing immersion time.[82j]

Formation voltage:

Soft organic SEI and hard inorganic SEI were found to form at higher and lower potentials, respectively.[19, 96a] Moreover, adjusting the discharge cut-off voltages to control the dissolution of SEI effectively improved the stability of Si anode.[32b]

Lithiation state:

Distinct SEIs were observed as the lithiation states vary.[28, 111b] Specifically, in both electrolytes with and without the additive of fluoroethylene carbonate (FEC) in 1.2 M $LiPF_6$/EC- (ethyl methyl carbonate) EMC, the viscosity and shear modulus of SEI were found to increase and decrease with the lithiation state of Sn anode, respectively.[28]

Reaction rate:

In 1 M $LiClO_4$/EC-DMC, the uniformity and coverage of SEI on graphite anode decreased with increasing voltage scan rate.[18] A large current density may induce amorphization of the LiF layer and increased the bond integrity of SEI;[4b] it can also reduce the repair time of SEI and thus decrease its protectiveness.[113]

Cycle number:

Multiple properties of SEI, including chemical composition,[19-20] resistance,[19] modulus,[19, 43a] structure,[66a] thickness,[20, 32b] and surface roughness,[20] were reported to vary with increasing number of cycles. Sometimes a stable SEI was formed within the first 20 cycles,[82a] and sometimes the properties of SEI continued to change even after 200 cycles.[20]

Temperature:

The temperature dependence of morphology and composition of SEI stems from (i) the different thermal stabilities of SEI components and (ii) the different temperature dependence of the electrolyte decomposition reactions. For example, when the temperature is increased, the decomposition of $ROCO_2Li$ in SEI is enhanced, leading to an increase in the porosity of SEI.

Elevated temperature also promotes the reaction of electrolyte salts, resulting in higher LiF content in SEI.[115]

Different position of electrode:

In-situ AFM characterisation of patterned silicon anodes revealed that the SEI formed at the center and in the shear hysteresis region of the silicon island had different properties.[7b]

In this section, we summarise related work on the mechanical characterisation of SEI using the AFM-NT method. We highlight operation details that need to be considered to improve test accuracy. It is also pointed out that the dynamic nature of SEI must be considered when comparing the mechanical properties of SEI between different battery systems. In future work, the characterization of SEI would preferably include different lithiation stages, number of cycles, and dry/wet test environments. Furthermore, in view of the large dispersion of current test results, a valid discussion must be based on a large amount of experimental data obtained from different positions of the electrodes.

6.2.7 Suggestions on sample preparation for AFMNT tests

Since SEI on alkali metal anodes is highly sensitive to the environment, to obtain high precision results from AFMNT test, we first recommend that the AFM instrument be encapsulated in a glove box that allows precise monitoring and control of the atmosphere. The disassembly of the battery, the cleaning and drying of the electrode sheets to be tested are also preferably done in the glove box where the AFM is located to reduce the oxidative denaturation of SEI during the sample transfer process. Finally, most AFMNT tests are performed on dry electrodes, but considering that the actual deformation of SEI occurs in the electrolyte, it is highly recommended that future AMFNT tests of SEI be performed in the electrolyte. In this case, close attention needs to be paid to the volatilization of electrolytes. Because as the electrolyte evaporates, the increase in electrolyte concentration and viscosity may influence SEI mechanics.

7 Efforts to enhance the mechanical properties of SEI

To boost the cycling performance of batteries, many research efforts have been carried out to improve the mechanical stability of SEI. The research work is reviewed below in terms of the target mechanical properties of SEI, including modulus, coverage or film-forming ability, elastic strain limit, thickness, and uniformity. Due to the large number of articles devoted to SEI optimization, those that only mentioned mechanistic concepts without providing experimental data are skipped in the following discussion.

7.1 Large modulus

It is pointed out in section 4 that theoretical analysis indicated that a high modulus SEI could more effectively suppress dendrite growth and the occurrence of wrinkling and ratcheting on the SEI, thus benefiting the stability of battery. In this section, we summarize the related experimental work on optimizing battery performance by increasing the modulus of SEI.

7.1.1 Electrolyte additive

One of the main categories is the addition of functional electrolyte additives to the electrolyte. The addition of VC in 1 M $LiPF_6$/EC-DEC greatly increased the shear storage modulus of SEI due to the precipitation of compact cross-linked polymeric compounds such as poly(VC)) and rigid inorganic species such as Li_2CO_3.[91c] The additives of FEC in 1 M $LiPF_6$/EC-DEC,[91c] 1 M $LiPF_6$/EC-EMC[82f], 1.3 M $LiPF_6$/EC-DEC,[116] and 1.2 M $LiPF_6$/EC[30] electrolytes have been reported to increase the modulus of SEI on carbon/highly oriented pyrolytic graphite (HOPG) anode, probably due to the increased content of LiF at the anode interface.[91c, 116] A dual additive of FEC and LiDFOB in LiFSI/DME - 1,1,2,2-tetrafluoroethyl 2,2,3,3-tetrafluoropropyl ether (HFE) formed high modulus SEI rich in fluoride (F) and boron (B) on silicon anode.[82g] The addition of 5% trimethoxysilane to 1 M $LiPF_6$/EC-DMC improved the content of OPF_x compounds in SEI, which enhanced the covalent bonding of the silicon surface and other SEI components and led to a higher contact stiffness of SEI.[23]

7.1.2 Electrolyte formulation and voltage control

Modulation of electrolyte formulation is another widely adopted method to tune properties of SEI. Electrolytes with high concentrations of LiFSI (2 M LiFSI/DME,[69l] 3.85 M LiFSI/tetrahydrofuran (THF)[117]) formed LiF-rich SEIs with larger Young's modulus values. The electrolyte of 2.2 M LiTFSI + 0.2 M $LiPO_2F_2$/FEC-HFE boosted the battery performance due to the formation of a high modulus SEI with a dense Li_2O and LiF rich inner layer and an organic rich outer layer.[82i] Furthermore, when the electrolyte was changed from 1 M $LiPF_6$/EC-DMC to 1 M $LiPF_6$/FEC-DMC, a harder, denser LiF-rich SEI was formed.[82d] Modulus of SEI can also be controlled by regulating the formation voltage. For example, the SEI formed in 1 M $LiPF_6$/EC-DMC on Si thin film at 0.2 V had a larger *E* than at 0.4 V.[96a]

7.1.3 Artificial SEI

Apart from manipulating the electrolyte composition to impact in-situ formed SEIs, the anode surface can also be pre-treated with chemical solutions or self-supporting films to build artificial SEIs targeting large moduli.[69k, 118] For instance, an A-SEI dominated by Li_3PO_4 with high Young's modulus was formed by immersing Li metal anode in polyphosphoric acid (PPA) solution.[119] Spontaneous in-situ polymerization of 2,3,7,8-tetrakis((trimethylsilyl)

ethynyl)pyrazino[2,3-g]quinoxaline-5,10-dione (PPQ) also formed a high Young's modulus A-SEI.[69j] Treatment of graphite anode with the solution containing polyethylene glycol tert - octylphenyl ether (PEGPE) and polyethylene resulted in the formation of A-SEI with high mechanical strength due to the strong hydrogen bridge bonding between the two polymer components. The π–π interactions between the aromatic ring of PEGPE and the graphite surface also caused strong adhesion between the A-SEI and anode surface.[98] In some cases, the pre-formed A-SEI on the anode surface does not prevent the formation of natural SEI during cycling. In this case, the A-SEI and the subsequent natural SEI served as the inner and outer layers of SEI, respectively. An example is that the exposure of Li to Spiro-O8 solution formed a layer of phenoxy Spiro-O8-Li as the inner SEI. In addition, the phenoxy radicals on surface of Spiro-O8 promotes the decomposition of Li salts and leads to a LiF-dominated outer SEI.[62] Similarly, treating expanded graphite anode with dopamine hydrochloride solution yields an A-SEI consisting of inner polydopamine and outer natural SEI.[82h]

Covalent organic frameworks (COFs) with good mechanical strength are the rising star of A-SEI. The Young's modulus of COF is mainly dependent on its covalent frameworks and crystallinity, and can be tuned by adjusting the types and arrangement of functional groups of monomer molecules.[69d] In situ reactions between 2,4,6-triformylphloroglucinol (Tp) and p-phenylenediamine (Pa)[69d], as well as between 1,3,5-tris(4-aminophenyl) benzene (TAPB) and terephthaldehyde (PDA)[69e] both self-assembled into 2D COFs with high Young's modulus. Alloy-based SEI is another upward trend in A-SEI. Processing the Li metal anode with $AlCl_3$ ionic liquid produced a high-strength A-SEI layer, whose main components are Al-Li alloy and LiCl.[69b] Immersing Li metal anode in 1 M $LIPF_6$/EC-DEC+ SnF_2 (3 wt%) also yielded an A-SEI composed of LiF, Sn–Li alloy, and Sn, which had a high value of Young's modulus.[120] Atomic layer deposition (ALD) or molecular layer deposition (MLD) are also commonly used methods to prepare A-SEIs, which are suitable for depositing protective coatings of inorganic metal oxides and organic polymers, respectively. The thickness and uniformity of A-SEI prepared using these two methods can be precisely controlled.[33b, 121] Recently, researchers added trimethylaluminum (TMA) to promote the cross-linking between polymer chains when using MLD to prepare poly urea film, which greatly improved the stiffness of A-SEI and the stability of Li metal anode.[33a]

7.2 Large deformability

The SEI with a high ε_Y could increase the capability in accommodating the volume change. A glyme-based electrolyte (LiFSI – DME - 1,1,2,2-tetrafluoroethyl- 2,2,3,3-tetrafluoropropyl ether (TTE)) was reported to endow SEI with greater elastic deformability by increasing the

polyether content and decreasing the carbonate type content of the SEI.[37b] Electrolyte additives 5-methyl-4-((trifluoromethoxy)methyl)-1,3-dioxol-2-one (DMVC-OCF_3) and 5-methyl-4-((trimethylsilyloxy)methyl)-1,3-dioxol-2-one (DMVC-OTMS), increased the spatial flexibility and decreased the modulus of SEI via polymeric propagation with the vinyl group of VC.[99] The addition of sulfur-containing polymers to the electrolyte facilitated the formation of an inorganic/organic hybrid SEI layer, where the organosulfides/organopolysulfides functions as "plasticizer" in the inorganic phase to reduce Young's modulus of SEI and make it more flexible and stable.[83b]

Flexible A-SEIs have also been widely reported. The voltage-controlled electrochemical oxidation and polymerization of 1,3-dioxolane (DOL) precursor with LiTFSI additive on Li metal surface generated short chain oligomers of poly(ethylene oxide) to form an elastomeric A-SEI.[122] According to the surface chelation strategy, an organophosphorus hybrid flexible A-SEI was generated by treating Li metal surface with phytic acid. The mechanical flexibility of A-SEI was ensured by the polynuclear complex between the phytic acid and Li^+, which acted as a "connecter" within the SEI layer.[123] The in situ interfacial reaction between Li metal and ammonia borane produces lithium aminoborane. Within these [LiNBH]n chains the strong and numerous intermolecular Li-N ionic bonds allow for further cross-linking and self-reinforcement, resulting in a flexible polymer-like A-SEI.[124] The Li polyacrylic acid (LiPAA) gel polymer is highly stretchable (582% strain to its initial length) and can be prepared as the dominating component of A-SEI by the in situ reaction between Li metal and polyacrylic acid (PAA).[33c] The A-SEI composed mainly of polyamide (PA) and zinc trifluoromethanesulfonate ($Zn(TfO)_2$) which had a low crystallinity demonstrated sufficient viscoelasticity and flexibility to adjust to the mechanical stress produced during cycling due to its unique hydrogen-bonding network.[97b] A freestanding carbon film A-SEI prepared by electrospinning and magnetron sputtering demonstrated excellent flexibility and can be restored to its original flatness after twisting and extrusion.[125] Copolymer poly(vinylidene-co-hexafluoropropylene) (PVDF-HFP) gel also demonstrated a super stretchability (dry state: 320% and wet state: 1000%) and high toughness.[126]

7.3 Homogeneity

The homogeneity of SEI is essential for the mechanical stability of SEI, however, yet it is difficult to directly characterize it experimentally. Most of the research conclusions claiming to improve the uniformity of SEI are often derived from Cyro-TEM images or SEM images of the SEI/anode, which are intuitive perceptions and qualitative judgments. For example, in many electrolyte systems, mainly ether-based and high-concentration electrolytes,[9a, 31j, 39a, 43b, 57-60,

[103a] amorphous SEIs with small and uniform thickness without significant inclusion phases were observed. TEM images provide strong evidence of the SEI structure, with the only drawback being the small size of the sample imaged. Some recent works based on in situ electrochemical (EC)-AFM provide a good research approach to study the homogeneity of SEI. That is, by using anode materials with absolutely smooth surfaces, such as ultra-flat monolayer molybdenum disulfide prepared by chemical vapor deposition (CVD),[127] highly oriented pyrolytic graphite (HOPG),[128] etc., the interference of anode surface roughness on evaluation of SEI properties can be eliminated. In this way, the morphology, mechanics, electrical conductivity and other data obtained from AFM scanning can be used to quantify the uniformity of SEI.[129] This method is well suited to investigate the effects of electrolyte formulations and charge/discharge protocols on the properties of SEI. It should be noted that the surface morphology of the anode should not change unpredictably during the cycling process in the experiment, otherwise it will bring a large error in the evaluation of the SEI performance.

7.4 High coverage or film-forming capability

The film-forming ability of SEI is another important factor in determining the battery's cycling performance. The amount of electrolyte consumed to form a complete SEI covering the anode is largely dependent on the film-forming capability of SEI.[130] In addition, a cohesive SEI layer can well spread the external loads, reducing the risk of failure induced by stress concentration. Atomic reaction simulations using a hybrid Monte Carlo/MD reaction approach showed that the intact FEC molecules enhanced the network formation of organic species due to the large electronegativity of their fluorine atoms.[131] The PEO-like oligomers, produced by introducing the film-forming additive of DOL in the electrolyte was found to be beneficial in accommodating the volume deformation and maintaining the structural integrity of SEI.[130b] The reduction of FEC yielded vinoxyl radical which initiated both the chain reaction of the FEC decomposition and the polymerization of reaction products. The resulting polymers were further defluorinated to produce internal radicals which migrated and recombined to form a highly cross-linked network.[132] The boric acid (BA) was demonstrated as an effective SEI-forming additive in Li-O_2 batteries. Components like lithium borate, lithium carbonate, lithium fluoride, and some organic compounds of SEI are covalently bonded with BA by forming O-B-O bonds and thus greatly improve the cohesiveness of SEI.[133] Compared with the SEI formed in VC-free electrolyte, the SEI formed in the electrolyte containing 2 wt% VC was thicker, more uniform, and had much greater coverage on the Si anode.[26] A hybrid LiF/h-BN film served as excellent A-SEI for Li metal anode. The h-BN film prepared by CVD had a high theoretical in-plane Young's modulus. In contrast, the grain boundaries and point defects

worked as weak points and greatly decreased its mechanical strength. The selectively deposited LiF at these defected positions by the ALD method successfully seamed the h-BN film and enhanced the cycling performance of the battery.[134]

7.5 Combined increment of stiffness and flexibility

The assignment of strength and flexibility functions to different components of SEI was considered as a way to enhance both properties simultaneously. The action mechanism of many bilayer-SEIs is based on this argument. The SEI formed on Sn@PEO electrodes had an inorganic outer layer that provided passivation and an organic inner layer that accommodated the deformation and increased the toughness of SEI.[31f] In another case, the inner crystalline LiF layer provided the necessary mechanical hardness and high interfacial energy with the Li metal and the outer Li - bis(2-methoxyethyl) aminosulfide (MAS) organic layer enhanced the flexibility and functioned as a stress-release layer.[47] Similarly, a bilayer A-SEI consisting of organic alucone as the outer layer and inorganic Al_2O_3 as the inner layer was fabricated by ALD and MLD methods. The dense and hard Al_2O_3 layer passivated the anode surface and the porous and highly flexible alucone layer allowed electrolyte diffusion and relieved the volume change of Li metals during cycling.[33b]

Besides the bilayer-SEI, A-SEI with composite structure was another main category to achieve combined improvement of stiffness and flexibility. Composited A-SEIs typically consist of a soft/flexible matrix in which hard particles are distributed. The incorporated particles provide the required mechanical stiffness to inhibit dendrite growth or crack nucleation, while the matrix provides flexibility and maintains the integrity of SEI. A-SEIs with composite structure includes the Cu_3N particles in the SBR matrix,[55a] the ClO_4^--decorated metal-organic framework (UiO-66-ClO_4) with flexible Li-Nafion binder,[69a] the LiF powders embedded in the PVDF-HFP matrix[90d], the LiF incorporated poly-methacrylate,[135] and mesoporous SiO_2 filler in polyvinylidene difluoride (PVDF) matrix[136].

7.6 Summary

We summarise in **Figure 8**a and 8b the percentage of the various methods employed to optimise the mechanical properties of SEI. The construction of A-SEIs is the most used method in metal batteries, while the adjustment of electrolyte composition is the most popular approach for metal-ion batteries. This difference may be due to the rough and irregular shape of active materials in metal-ion battery anodes, and the presence of conductive agents and binders that impair the functionality of A-SEI and have less effect on the high-quality SEI formed by electrolyte tuning. As can be seen from Figure 8c and 8d, nearly half of the efforts to tune the mechanical properties of SEIs have been focused on improving the Young's modulus of SEIs,

regardless of metal batteries or metal-ion batteries. One reason for this is that parameters related to deformability, such as the elastic strain limit, are specific points on the stress-strain curve relationship, whereas Young's modulus is the value of the slope of the elastic section of the stress-strain curve. The latter is easier to measure with lower requirements for experimental testing.[10a, 29-30, 31j] Therefore, modulus values for SEI are widely available in works studying the mechanical behaviour of SEI while values for specific strain are rarely seen. It is desirable to generate a complete SEI stress-strain curve as shown in Figure 4a. This not only offers us a comprehensive understanding of the mechanical behaviour of SEI, but also improves the accuracy of theoretical simulations using these parameters.

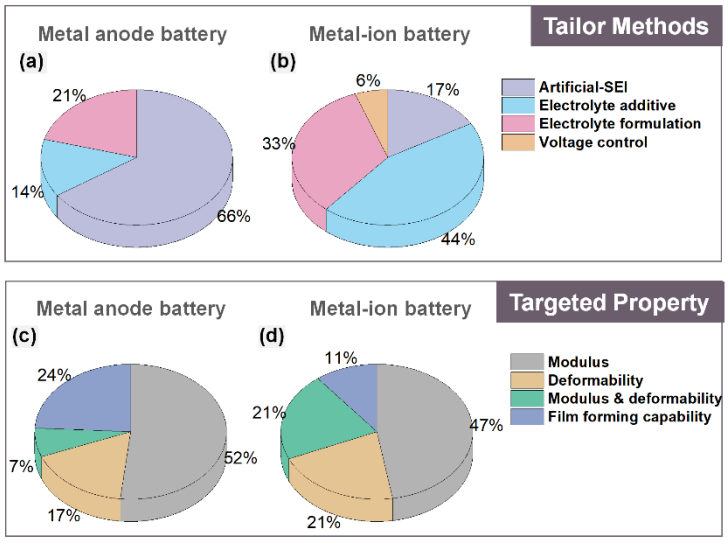

Figure 8. Optimization of SEI mechanical properties. Percentages of different tailor methods to achieve better mechanical properties of SEI for (a) metal anode battery and (b)metal-ion battery, respectively. Percentages of targeted mechanical properties of SEI for (c) metal anode battery and (d) metal-ion battery, respectively.

8 Discrepancies and causes

In addition to the trade-offs in values of E and ε_Y for SEI discussed earlier in section 4.2, other major areas of disagreement are the definitions of the beneficial components in SEI and the required level of adhesion between SEI and anode. The absence of unified viewpoints in these areas can greatly hinder subsequent development. Therefore, in this section, we summarize the current controversies related to the mechanical properties of SEI and speculate on the reasons for these controversies.

8.1 Discrepancies

8.1.1 The role of organic components

The organic species in native SEI is mostly described as soft, porous, dissolvable, easily pierced by dendrite, and is generally considered unfavourable for mechanically stable SEI.[82i, 101]

However, there are also articles showing that organic substances, especially polymers, act as a buffer layer and provide the necessary flexibility of SEI to accommodate the anode deformation.[37b, 99, 137] Furthermore, under conventional cycling conditions, it is difficult for pure inorganic constituents to form a continuous film without organics as connectors. For example, several articles have shown that the beneficial effect of FEC in enhancing cycling performance stems from their ability to promote the formation of cross-linked organic networks.[64b, 131-132]

8.1.2 The role of inorganic components, especially LiF

The unique properties of bulk LiF or Li_3N, including high mechanical strength,[138] low solubility,[139] wide electrochemical stability window,[140] high interfacial energy,[141] and low electron conductivity,[142] make them considered important SEI components to achieve uniform Li^+ flux and suppress dendrite growth.[143] SEI with more LiF was always perceived as having a higher modulus and therefore a higher resistance to dendrite growth.[69l, 82d, 116-117] Additionally, first principle simulations showed that with sufficient Li bias at the LiF-Li_xSi interface, LiF would bind to Li_xSi and increased the ductility of SEI by forming dispersed stable voids in the interfacial region.[144]

However, there are also numerous reports that the presence of LiF or other inorganic salts is harmful to the cycling stability of SEI. For example, the SEI formed in PC-based electrolytes was rich in LiF but had poor cycling performance.[145] The SEI formed on the graphite anode in EC-DMC electrolyte mainly consisted of inorganic Li salts. It was inflexible, less cohesive and unable to provide sealing and absolute protection for the anode.[4c] Furthermore, the decreased LiF content on the surface of Si anode after adding VC, FEC, LiBOB, and LiFOB in 1 M $LiPF_6$/EC-DMC-DEC electrolyte was regarded as a reflection of the success in suppressing the decomposition of $LiPF_6$.[145] A layer of LiF was formed on Cu by ALD method to evaluate its intrinsic behaviour. However, the strong chemical bond between LiF and Cu reduced the nucleation sites for Li, resulting in Li deposition between LiF particles instead of underneath them.[134] As a result, a more inhomogeneous Li deposition was observed with the LiF coating than the pristine Cu surface. Moreover, pre-formed and naturally formed LiF-rich SEIs were found to have difficulty maintaining their structural integrity during cycling. It was concluded that the superior performance of the battery was not attributed to the LiF content, but that the FEC in the electrolyte can continuously repair the SEI with additional LiF or form an elastic outer layer.[31k]

8.1.3 The degree of adhesion between SEI and anode

The strong adhesion between SEI and anode is considered advantageous in two main respects. One is that the smaller adhesion makes it easier to remove the SEI component from the anode surface during the initial formation of SEI. As a result, more electrolytes would be consumed to form a complete SEI film with passivation capabilities.[21, 67, 130a] SEIs formed in this way were typically thicker and less uniform. The other is that when a localized penetrating crack occurs in the SEI, weak adhesion can lead to delamination and flaking off of the entire SEI, resulting in a significant drop in CE or cell failure.[69i, 146] The beneficial effects of strong bonding between SEI and anode have been confirmed by many simulation and experimental results.[23, 33c, 52, 69h, 98, 125b] For example, theoretical calculations showed that a thin SEI with considerable interfacial energy better avoided debonding under the large radial tensile stress generated during the delithiation process.[70] Moreover, artificial SEIs with strong adhesion to the anode,[33c, 69i] e.g. by forming π-π interaction,[98] or covalent bonds like Li-O-Si[146b] and Ti-Si[146c], demonstrated effectiveness in achieving outstanding cycling stability.

The reason for preferring a weak bond between SEI and anode is that a strong bonding interface causes the SEI to experience the same degree of deformation as the anode, more easily reaching the critical point of the SEI's deformability and failure. In contrast, the low adhesion between SEI and anode allowed the anode to be repositioned and therefore able to accommodate volume changes and introduced minor damage to the SEI shell.[9b, 47, 54] In addition, as we mentioned before, the strong bond between SEI and metal anode may also make it challenging to form Li nucleation sites and worsen the deposition behaviour in Li metal anode.[134]

8.2 Causes of these discrepancies

This section attempts to unravel the reasons and mechanisms behind these seemingly contradictory statements.

8.2.1 Different structures of components

The mechanical properties of a chemical substance are not constant but are highly sensitive to its structure. The controversy over the mechanical properties of SEIs with the same components may be partly because these seemingly identical chemistries actually have different structures.

Crystalline or amorphous:

MD simulations showed that, for the same material, the Young's modulus of the amorphous structure was lower than that of the crystalline structure. For example, crystalline LiF had a Young's modulus of 135.3 GPa and exhibited brittle fracture. While, amorphous LiF had a Young's modulus of 58.1 GPa and exhibited ductile fracture. Similarly, the Young's modulus of Li_2CO_3 with crystalline and amorphous structure was also distinctly different, 54.8 and 36.2

GPa, respectively.[82b] The results of MD and hybrid MD-Monte Carlo schemes showed that the modulus of organoLi salts was also influenced by the degree of ordering of their structures. For example, when the structure of the decarbonated butyl Li changed from an ordered to an amorphous state, its shear modulus increased from 1.4 to 2.1 GPa.[147]

Different chain lengths of organic species:

Both simulation and experimental results suggested a dependence of mechanical properties of organic species on their chain length. MD simulations indicated that ordered dilithium ethylene decarbonate (Li_2EDC) and dilithium butylene decarbonate (Li_2BDC) phases had highly anisotropic mechanical properties. Increasing the length of alkyl spacers between the carbonate groups on the anion would form more defined Li^+ layers and show a reduction in shear strength along the plane of formed layers.[147] A series of homologous Li alkyl carbonates (LiACs) and Na alkyl carbonates NaACs were experimentally synthesized, and their Young's moduli were characterized by AFM-NT method. As the x in C_xLi/C_xNa (referring to the C/Li ratio in alkyl carbonates) increased from 1 to 8, Young's modulus of LiACs changed slightly, while that of NaACs decreased significantly from 1.2 GPa to 0.3 GPa.[79]

Whether organic species are copolymerized/cross-linked:

The SEIs with abundant polymeric or cross-linked networks generated by additives such as FEC,[114a, 148] VC[99] and boric acid[99] were believed to have higher mechanical strength[133, 149] or deformation accommodation capability[99] than traditional linear oligomeric species generated from electrolyte reduction. Highly cross-linked COF-based A-SEIs had Young's modulus as high as 6.8 GPa.[69e, 138a] The strength of hydrogen bond (H-bond) was also found to affect the mechanical properties of polymers. A series of polymeric coating materials with the same polymer backbone and tunable H-bond strength were synthesized and mechanically characterized. The polymer with higher H-bond strength had a more ordered structure and behaved like a viscoelastic solid. The polymer containing lower H-bond strength behaved like viscoelastic liquid and resulted in a higher CE value due to their better flowability or faster polymer dynamics.[97a]

8.2.2 Different structures of SEI.

In addition to the various structures of the chemicals themselves, the way they are arranged in the SEI, i.e., the structure of the SEI, also has a substantial influence on the mechanical properties of the SEI. Discussing the relationship between the components and properties of SEI in isolation from the SEI structure often leads to disagreement.

The properties of individual components do not represent the overall properties of SEI:

The composition of SEI is complex and always contains various phases. The mechanical properties of individual components are not representative of the overall performance of SEI. In the absence of mechanical testing, simply assuming that increasing the content of certain components of SEI will improve its mechanical properties introduces a high degree of uncertainty.

Care must be taken when extrapolating properties of individual compounds to the properties of complex mixtures, one reason is that compounds in mixtures may behave differently than pure substances.[79] The final manifested properties of a multi-component SEI are influenced by a number of factors, including the morphology (crystalline/amorphous and particle size), distribution (concentrated/homogeneous), location (inner layer/outer layer/multi-phase junction) and interactions with other components (**Figure 9**a).[150] It was experimentally observed that even in SEI containing large amounts of LiF (molar ratios of about 20~50 %), LiF did not form solid films but existed as isolated domains or crystals of considerable size.[115] In this case, the increasing effect of LiF on the SEI modulus is greatly weakened. For example, the Young's moduli of pure PVDF-HFP film and LiF are 0.8 GPa and 135.3 GPa, respectively.[82b] The Young's modulus of the composite film with LiF powders uniformly distributed in the PVDF-HFP matrix (with a mass ratio of 1:2) was only 6.72 GPa.[69h]

Although the inorganic inclusion phase in the SEI with a composite structure increased the overall modulus of SEI, the large size of inorganic particles and their inhomogeneous distribution in the matrix phase reduced the elastic strain limit of SEI.[10b, 115] Therefore, there is an optimal content of inorganic salts to maximize the mechanical stability of SEI. The value of the optimum content is affected by the particle size of the inorganic matter and the degree of dispersion uniformity. When the inorganic salt particles are sufficiently small and uniformly distributed that the SEI can be regarded as a single-phase material, the advantages of the inorganic inclusion phase are maximized and the disadvantages are minimized.[57, 59-60] The optimum content of inorganic component will then be much higher than the value for heterogeneous SEI.

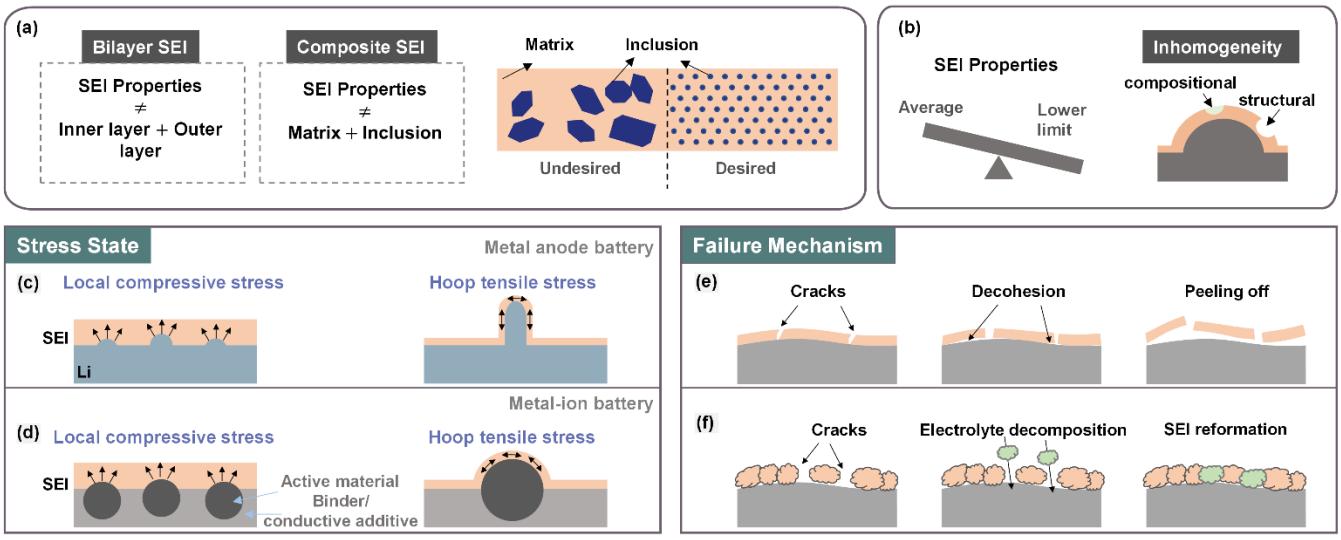

Figure 9. Causes of discrepancies. (a) The performance of SEI is not simply the sum of the performance of constituent components. (b) Inhomogeneity of SEI makes the cycling performance of battery tend to be related to the lower limit of the mechanical stability of SEI rather than the average value. Illustrations of possible stress state for (c) metal anode battery and (d) metal-ion battery, respectively. Different failure mechanisms of (e) cohesive SEI and (f) poor cohesive SEI, which affect their preference for the degree of adhesion between SEI and anode.

Relationships between monolayer performance and the overall performance of bilayer/multilayer SEI:

A common but less accurate view of bilayer/multilayer SEI is that the inner dense inorganic layer provides the mechanical strength required to inhibit dendrite growth, while the outer organic layer provides the required flexibility to accommodate the large anode deformation during cycling. This synergistic effect of inorganic and organic components can be achieved in SEIs with composite or monolithic structures, but is more difficult in SEIs with bilayer/multilayer structures.

First, for alloy anodes in metal-ion batteries, each layer of SEI is subject to anode deformation. The difference is only the deformation degree, which mainly depends on the curvature of the electrode surface or the active particles. For metal anodes, the inner layer of SEI experiences a higher level of stress than the outer layer during the nucleation stage of metal plating. However, once dendrite growth occurs, the deformation difference experienced by the inner and outer layers of SEI rapidly decreases.

Secondly, under ideal circumstances, as long as one of the SEI layers is not damaged, its protective capacity can be maintained. In practice, however, the situation is much more complicated. For the case where the inner layer of SEI is broken and the outer layer retains its

protective properties, new SEI elements cannot be formed to repair the damaged inner layer. Since the electric field at the fracture site would be localized enhanced, the cracking of SEI will intensify in subsequent cycles, eventually leading to the failure of the outer layer of SEI. For cases where the inner layer is broken and the outer layer cannot provide complete passivation (probably due to its porous structure), new SEI elements are formed. The consumption of electrolytes and charges during the repair process reduces the CE and possibly increases the thickness and impedance of SEI.

Therefore, each layer of the bilayer/multilayer SEI needs to have sufficient mechanical stability, otherwise the cycling stability of the battery is mainly determined by the most stable layer of SEI. The experimentally observed excellent mechanical stability of the bilayer SEI may be because one of the layers of SEI is super stable or that the structure of SEI is not strictly a bilayer but a gradient composite.

8.2.3 Inhomogeneity of SEI exaggerates its shortcomings.

As we summarized in Table 1, many mechanical characterisation methods can only provide average values for the tested properties of SEI. While for SEIs with heterogeneous structures, the average value is insufficient to describe their true behaviour during cycling. The failure of SEI is usually a local rather than a global behaviour. The mechanical properties at the failure location of SEI may not be represented by the average value of SEI properties, but closer to the lower limit (Figure 9b). In the future characterization of mechanical properties of SEI, it is strongly recommended to provide more information on the distribution of the data. Statistical analysis of the data can be used to assess the homogeneity of SEI and is also crucial for comparing two systems with similar mean values.

8.2.4 Desired mechanical property varies with the stress state and failure mechanism of SEI.

The maximum elastic strain energy (*U*) of SEI has been suggested to predict its stability during cycling. When the stress state of SEI changes, the expression of *U* also changes. For example, under the internal pressure generated by the cell encapsulation, the growth of metal atomic clusters on the metal anode (Figure 9c) and the initial lithiation expansion of the alloy anode particles (Figure 9d) can place the SEI in a stress state that approximates local indentation. In the previous articles that discussing *U* of SEI, the stress state targeted were all this local indentation condition, and the expression of *U* is listed below[10a]:

$$U = \int_0^{d_c} Fd(d) = \frac{8}{15}\left(\frac{4}{5}\pi\right)^5 \cdot r^3 \cdot \frac{E^5}{\left(E_r^0\right)^4} \cdot (\varepsilon_Y)^5 \propto E \cdot {\varepsilon_Y}^5 \quad (16)$$

where E_r^0 equals $E/(1-\nu^2)$ for a rigid indenter, ν is the SEI's Poisson's ratio, and r is the radius of the rigid indenter. Simply put, the value of U is proportional to $E \cdot \varepsilon_Y{}^5$. However, if the SEI on the alloy anode particles is relatively thin, or if there are fast-growing dendrites on the metal anode, the stress state of SEI becomes very different. For example, the stress states of SEI over uniformly expanded alloy anode particles and the SEI at the top of dendrites on metal anodes resemble hoop stress, with force components both parallel and perpendicular to the SEI thickness. On the other hand, the state of SEI at sidewalls of dendrites is close to uniaxial stretching, i.e., the force perpendicular to SEI thickness dominates. The SEI at the root of the dendrites is susceptible to stress concentration and its stress analysis is very complex. The expressions of U for the stress states will be quite different from **Equation 16**. The above conclusions are for the simplified extreme cases and assume that SEI is a homogeneous material. The actual situation will be more complex and variable, resulting in different electrode-electrolyte systems may have different propensities for E and ε_Y.[151]

Furthermore, SEIs with different structures can have different failure mechanisms during cycling.[152] This may explain the controversy over the ideal level of adhesion between SEI and anode. For highly cohesive SEI films, the weak adhesive strength at the SEI/anode interface may lead to extensive SEI exfoliation from the anode once penetrating cracks occur (Figure 9e). In contrast, for SEI with a mosaic structure dominated by less cross-linked inorganic components, local cracks in the SEI will not lead to the detachment of large-area SEI due to the weak bonding between adjacent SEI phases (Figure 9f). In this case, the disadvantage of low SEI-anode adhesion is reduced and its advantage of accommodating large deformation is amplified.

8.2.5 Coordination between SEI mechanical properties and other properties

Besides mechanical properties, many properties of SEI also affect its stability during cycling, such as the film-forming ability, ion transport ability, uniformity, chemical stability, temperature stability, etc.[153] During battery cycling, stressors that cause SEI rupture include volume expansion of alloyed anode materials, uneven metal deposition and dendrite growth on metal anodes, thermal stress caused by local/environmental temperature changes and so on. If the SEI thickness is uniform, the film formation is good, the ion transport is fast and uniform, the initial surface of the metal anode is flat and smooth, and the volume deformation of the alloy anode during lithiation is small and isotropic, all of which reduce the stresses faced by the SEI during cycling. Whether an SEI breaks or not depends on the relative relationship between the stress it actually bears (mainly influenced by other parameters) and the stress it can bear (determined by its mechanical properties). Therefore, improving the stability of SEI can be

done in two ways, either by adjusting other properties or cycling conditions to reduce the actual stress faced by the SEI, or by optimizing the mechanical properties of SEI to increase the stress limit it can withstand. The mechanical stability of SEI can be achieved as long as the SEI can withstand a higher stress value than it actually bears. That is to say, after satisfying this relative relationship, there is no need to infinitely improve its mechanical properties.[31l, 154] A common difficulty encountered in practical operation is that when a certain property of SEI is adjusted and optimized, another property may be degraded. For example, thicker SEIs are mechanically beneficial but detrimental to ionic conductivity. Therefore, in most cases, parametric studies are very important for optimizing battery performance.

9 Suggested methodology for investigating mechanical properties of SEI

The above discussions imply that incomplete studies of the mechanical properties of SEI easily lead to disagreements and misjudgements, thus decreasing their effectiveness in guiding future SEI designs. Most research work focused on improving battery performance has directly constructed relationships between the chemical composition of SEI and the battery cycling performance, without providing information on the microstructure and mechanical properties of SEI. This has the potential to lead to a misunderstanding of the true action mechanism. For research work that focuses on SEI mechanics, information on the structure of SEI is still sometimes omitted, thus reducing the generality of the conclusions.[69l, 82c, 82d, 83a] To deepen our understanding of SEI mechanical properties and to provide actionable design strategies, we suggest a research protocol shown in **Figure 10** for future investigations.

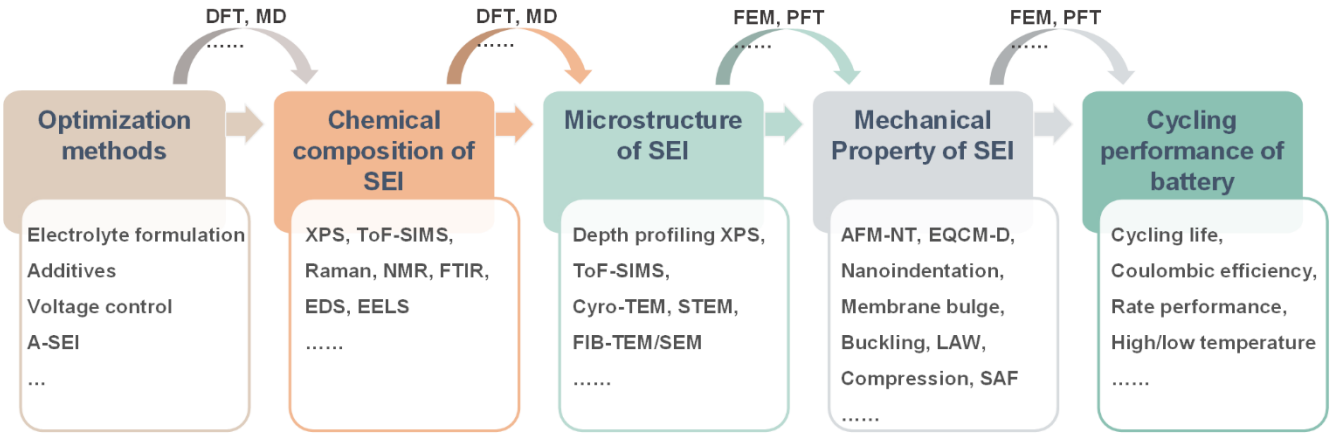

Figure 10. Research logic chain. Suggested methods for the investigation of mechanical properties of SEI.

Necessary experimental results such as chemical composition, structure, and mechanical properties of SEI, and corresponding battery cycle performance should be provided. The absence of any partial information listed in Figure 10 reduces the validity of the conclusions. The kinds of errors that each test may introduce should be kept in mind. For example, the

content of Li_2CO_3 in SEI was highly dependent on the processing conditions of the sample.[32a] Ar^+ sputtering used in XPS depth profiling may lead to the decomposition of Li_2CO_3 and the generation of Li_2O and LiOH in SEI.[31c, 32a] The various operational details of AFM-NT test that we have summarized in section 6 should be addressed. In addition, it is strongly recommended to adopt multiple test methods, which can effectively minimize the impact of testing errors from a single approach, thereby improving the research accuracy.[155] For example, several methods among XPS,[104, 156] ToF-SIMS,[33, 157] nuclear magnetic resonance (NMR),[69d, 158] X-ray diffraction,[159] Raman,[20, 160] fourier-transform infrared spectroscopy (FTIR),[47, 69d, 158b] and electron energy loss spectroscopy (EELS)[64b] methods can be employed to characterize the chemical composition of SEI. Moreover, considering the dynamic characteristics of SEI, the mechanical investigation of SEI should preferably include different number of cycles and under wet and dry states.

Simulations are crucial to revealing the theoretical link between the compositional structure and mechanical properties of SEI, as well as the relationship between the mechanical properties of SEI and the battery cycling performance. Simulations are recommended to be carried out in the following order: first to verify or modify the initial theory suggested by the experimental results; then to perform simulations to identify deficiencies in the SEI studied and use it to guide future battery design; and finally to perform experiments to validate the optimisation directions indicated by the simulation and to further refine the control theory based on experimental feedback. In increasing modelling scale, common simulation methods include density function theory (DFT), MD,[161] PFT[154] and FEM. In addition, emerging machine and deep learning techniques show promise and advantages in multi-scale simulations.[162]

10 Perspectives

Constructing a mechanically stable SEI is crucial for achieving stable cycling of high-capacity secondary batteries. In this review, we outline the desirable mechanical properties of SEI and available characterization methods. We also summarize attempts to optimize battery performance by tuning SEI mechanical properties, clarifying the divergence of these efforts and the possible reasons behind them.

Finally, with regard to accelerating the achievement of superior battery performance by improving the mechanical stability of SEI, we propose potential research directions related to the following issues.

10.1 Deepen understanding of SEI

10.1.1 Mechanical characterization on cross-sections of SEI

SEI usually contains more than one chemical substance. The mechanical properties of these components vary widely. The way these substances are combined can greatly affect the final mechanical properties of the SEI. An in-depth understanding of the SEI structure not only helps to clarify its failure mechanism, but also helps to understand how the experimental conditions (e.g. electrolyte composition and formation potentials) affect the formation of SEI. At present, great progress has been made in decoding the composition and structure of SEI. For example, XPS depth profiling can provide chemical information at different thicknesses in SEI; ToF-SIMS[33, 157] and TERS[20] can present 3D compositional information of SEI; (Cyro-) TEM[34b, 39a, 64b, 101, 163] and EELS[64b] are able to provide structural details of SEI cross-sections.

However, a significant gap in our current understanding of SEI is that the measured properties of SEI often do not have a thickness-wise resolution. If the AFMNT test in the future can be performed directly on the cross-sectional samples of SEI, not only the mechanical properties of each phase, but also the mechanical performance at the interfaces between different phases can be directly understood. The homogeneity of SEI can also be more accurately evaluated based on distributions of thickness and compositional phases. Combined with other capabilities of AFM, such as electrostatic force microscopy (EFM) and Kelvin force microscopy (KPFM), our understanding of SEI will take a new step forward. Not only can we clarify the layered structure of SEI, but we can also determine the mechanical contribution of each component, identify the failure mechanism, and thus optimize the design in a more targeted manner. The nanoscale thickness and environmental sensitivity of SEI make it difficult to perform mechanical experiments on its cross-section. (Cyro-) FIB[18, 34b, 41, 110a, 134, 164] is a powerful instrument for creating well-defined cross-sections of SEI-anode samples for SEM[18, 41, 53, 110a, 134, 164] or TEM[34b] studies, and could be a promising method to prepare SEI cross-section samples for AFMNT test. Given that cross-sectional samples for mechanical testing do not require ultra-thin thicknesses, simpler tools may also be able to accomplish this task.

10.1.2 Failure mechanism identification of SEI

The failure mechanism of individual battery systems reflects the shortcomings and optimization directions of the system and should be a focus in battery research. In situ testing methods have irreplaceable importance in the detection of failure mechanisms.[5c, 151, 165] For example, in-situ electrochemical (EC)-AFM can provide the time-resolved morphology information of SEI.[4c, 31b, 82c-f, 130a, 166] In-situ SECM can reinforce the function of EC-AFM with additional information on the electrical conductivity of SEI and detection of electrolyte decomposition

products.[167] In-situ scanning transmission electron microscopy (STEM)[168] and TEM[169] can visualize Li's deposition and dissolution process. TERS with high enhancement factor and spectral resolution provides detailed information on the conformational changes in SEI species.[1a, 20] It should be remembered that the experimental conditions in the in-situ tests do not fully replicate the actual conditions of the battery. Whether this difference in the experimental environment, such as the relative positions of anode and cathode and the battery's internal pressure, affects the behaviour and mechanism of SEI is still a question that needs to be studied in the future.

10.1.3 Theoretical analysis of SEI mechanics

Currently, mechanical analysis of SEI is mainly limited to flat metal anode or spherical anode particles of ion batteries. In practice, the porous structure and irregular curvature of the coated electrodes, as well as the presence of binders and conductive additives, all affect the formation, distribution and stress state of SEI.[170] Therefore, the mechanical analysis of SEI still has a long way to go. In this regard, simulations can play an important role in detecting possible mechanisms.[171] Besides pure mechanical analysis, the study of the dynamic interactions between multiple physical fields (e.g. the electrical, chemical and mechanical) within a battery system is an important but less explored area.[154, 172] For example, the lithiation of alloy anode exerts an external force on SEI and the stiff SEI layer that surrounds the alloy anode also has an effect on its lithiation capacity.[70] The crack in SEI also affects the electrical field distribution and enhances ion diffusion in the cracked region, thereby exacerbating the inhomogeneity of subsequent lithium deposition and triggering dendrite growth.[10b, 69j] In addition, gaining an in-depth understanding of the interplay between lithium diffusion/deposition and the mechanical response of SEI helps to elucidate the desired properties of SEI under extreme test conditions, such as at high/low temperature and high current/capacity densities.[19] Simulation methods like PFT or FEM, as well as the experimental methods of EFM[69j] and SECM can all play an important role in studying the electrochemical-mechanical coupling phenomenon of the battery field.

10.2 Rational design and construction of SEI

10.2.1 Improving the homogeneity of SEI

Besides the suggested research protocol for each specific battery system, there are general optimization approaches applicable to all systems, such as improving the homogeneity of SEI. The homogeneity of SEI consists of two aspects: composition and structure. Improving the compositional homogeneity of SEI refers to that different components are completely mixed

with each other and that no obvious phase boundaries are created. Because from a purely mechanical point of view, while keeping compositions constant, the SEI with a monolithic structure has the largest mechanical stability. Electrolyte conditioning is currently a common method to achieve monolithic SEIs.[9a, 31j, 43b, 57-60]

Improving the structural homogeneity of SEI mainly means making the composition and thickness of SEI consistent at different locations of the anode. Considering that the SEI is composed of the reduction products of electrolytes, and the reaction process also depends on the electrical field distribution on the anode surface, constructing a flat and smooth anode surface should be an effective method to improve the uniformity of SEI. The smooth surface of metal anodes can be achieved by electrochemical polishing[31g] or mechanical methods,[33c, 173] preferably as a necessary processing step for every metal anode battery.

10.2.2 Building well-designed A-SEI

Another optimization method with broad applicability is the construction of artificial SEI (A-SEI). A-SEI has proven very effective in achieving high cycle stability battery performance.[8c, 174] Furthermore, the composition and structure of A-SEI are more controllable than naturally grown SEI (N-SEI). The study of the mechanical behaviour of SEI usually focuses on the last two steps in Figure 10, which have similar difficulty for A-SEI and N-SEI. While the optimization of the compositional structure of SEI is related to the first two steps in Figure 10, and the difficulty of N-SEI is significantly greater than that of A-SEI. The formation of N-SEI involves reduction reactions of various electrolyte components and interactions between reduction products and the anode surface. The precise regulation of SEI compositional structure depends on a thorough understanding and utilisation of the above-mentioned processes. And this is still very difficult. In contrast, A-SEI is usually prepared on the electrode surface before battery cycling, with fewer restrictions and higher precision in tuning thickness, structure and components of SEI.[175] Achievements and technologies from mature fields such as surface treatment or thin film preparation can also be incorporated into the development of artificial SEI. The construction of artificial SEI can even be extended to the fields of solid electrolyte or separator modifications.

Acknowledgements

This work was supported by the General Research Fund (GRF) scheme of the Hong Kong Research Grants Council [Projects No. 15301220], Guangdong-Hong Kong-Macau Joint

Laboratory [grant no. 2019B121205001], and the Hong Kong Polytechnic University (1-ZVGH).

Conflict of Interest

The authors declare no conflict of interest.

References

[1] a) A. K. Stephan, *Joule* **2019**, *3*, 1812-1814; b) E. Peled, S. Menkin, *J. Electrochem. Soc.* **2017**, *164*, A1703-A1719; c) H. W. Wang, D. Y. Zhai, F. Y. Kang, *Energy Environ. Sci.* **2020**, *13*, 4583-4608.

[2] B. Horstmann, F. Single, A. Latz, *Curr. Opin. Electrochem.* **2019**, *13*, 61-69.

[3] a) M. J. Du, K. M. Liao, Q. Lu, Z. P. Shao, *Energy Environ. Sci.* **2019**, *12*, 1780-1804; b) J. D. McBrayer, C. A. Apblett, K. L. Harrison, K. R. Fenton, S. D. Minteer, *Nanotechnology* **2021**, *32*, 502005; c) J. M. Reniers, G. Mulder, D. A. Howey, *J. Electrochem. Soc.* **2019**, *166*, A3189-A3200.

[4] a) J. Xu, R. D. Deshpande, J. Pan, Y.-T. Cheng, V. S. Battaglia, *J. Electrochem. Soc.* **2015**, *162*, A2026-A2035; b) D. E. Galvez-Aranda, A. Verma, K. Hankins, J. M. Seminario, P. P. Mukherjee, P. B. Balbuena, *J. Power Sources* **2019**, *419*, 208-218; c) M. Koltypin, Y. S. Cohen, B. Markovsky, Y. Cohen, D. Aurbach, *Electrochem. Commun.* **2002**, *4*, 17-23; d) K. Takahashi, V. Srinivasan, *J. Electrochem. Soc.* **2015**, *162*, A635; e) I. Laresgoiti, S. Kaebitz, M. Ecker, D. U. Sauer, *J. Power Sources* **2015**, *300*, 112-122.

[5] a) S. N. S. Hapuarachchi, Z. Q. Sun, C. Yan, *Adv. Sustain. Syst.* **2018**, *2*, 1700182; b) D. Atkins, E. Ayerbe, A. Benayad, F. G. Capone, E. Capria, I. Castelli, *Adv. Energy Mater.* **2021**, *5*, 202102687; c) S. Narayanan, J. S. Gibson, J. Aspinall, R. S. Weatherup, M. Pasta, *Curr. Opin. Solid State Mater. Sci.* **2022**, *26*, 100978.

[6] a) A. A. Tahmasbi, M. H. Eikerling, *Electrochim. Acta* **2018**, *283*, 75-87; b) S. J. An, J. Li, C. Daniel, D. Mohanty, S. Nagpure, D. L. Wood III, *Carbon* **2016**, *105*, 52-76.

[7] a) B. Breitung, P. Baumann, H. Sommer, J. Janek, T. Brezesinski, *Nanoscale* **2016**, *8*, 14048-14056; b) R. Kumar, A. Tokranov, B. W. Sheldon, X. Xiao, Z. Huang, C. Li, T. Mueller, *ACS Energy Lett.* **2016**, *1*, 689-697.

[8] a) W. Liu, P. Liu, D. Mitlin, *Adv. Energy Mater.* **2020**, *10*, 2002297; b) H. Yuan, X. Ding, T. Liu, J. Nai, Y. Wang, Y. Liu, C. Liu, X. Tao, *Mater. Today* **2022**, *53*, 173-196; c) P. Zhai, L. Liu, X. Gu, T. Wang, Y. Gong, *Adv. Energy Mater.* **2020**, *10*, 2001257.

[9] a) X. Cao, X. Ren, L. Zou, M. H. Engelhard, W. Huang, H. Wang, B. E. Matthews, H. Lee, C. Niu, B. W. Arey, Y. Cui, C. Wang, J. Xiao, J. Liu, W. Xu, J.-G. Zhang, *Nat. Energy* **2019**, *4*, 796-805; b) J. Chen, X. L. Fan, Q. Li, H. B. Yang, M. R. Khoshi, Y. B. Xu, S. Hwang, L. Chen, X. Ji, C. Y. Yang, H. X. He, C. M. Wang, E. Garfunkel, D. Su, O. Borodin, C. S. Wang, *Nat. Energy* **2020**, *5*, 386-397.

[10] a) Y. Gao, X. Du, Z. Hou, X. Shen, Y.-W. Mai, J.-M. Tarascon, B. Zhang, *Joule* **2021**, *5*, 1860-1872; b) Y. Gao, Z. Hou, R. Zhou, D. Wang, X. Guo, Y. Zhu, B. Zhang, *Adv. Funct. Mater.* **2022**, *32*, 2112399.

[11] D. N. Bennion, E. Littauer, *J. Electrochem. Soc.* **1976**, *123*, 1462.

[12] E. Peled, *J. Electrochem. Soc.* **1979**, *126*, 2047-2051.

[13] Y. Geronov, F. Schwager, R. Muller, *J. Electrochem. Soc.* **1982**, *129*, 1422.

[14] J. M. Thevenin, RH *J. Electrochem. Soc.* **1987**, *134*, 273.

[15] A. Zaban, E. Zinigrad, D. Aurbach, *J. Phys. Chem.* **1996**, *100*, 3089-3101.

[16] E. Peled, D. Golodnitsky, G. Ardel, *J. Electrochem. Soc.* **1997**, *144*, L208-L210.

[17] P. Lu, S. J. Harris, *Electrochem. Commun.* **2011**, *13*, 1035-1037.

[18] S. Bhattacharya, A. T. Alpas, *Carbon* **2012**, *50*, 5359-5371.

[19] A. Tokranov, R. Kumar, C. Li, S. Minne, X. Xiao, B. W. Sheldon, *Adv. Energy Mater.* **2016**, *6*, 1502302.

[20] J. Nanda, G. Yang, T. Hou, D. N. Voylov, X. Li, R. E. Ruther, M. Naguib, K. Persson, G. M. Veith, A. P. Sokolov, *Joule* **2019**, *3*, 2001-2019.

[21] D. Bar-Tow, E. Peled, L. Burstein, *J. Electrochem. Soc.* **1999**, *146*, 824.

[22] C. Monroe, J. Newman, *J. Electrochem. Soc.* **2005**, *152*, A396-A404.

[23] W. Xu, S. S. S. Vegunta, J. C. Flake, *J. Power Sources* **2011**, *196*, 8583-8589.

[24] J. Zhang, R. Wang, X. Yang, W. Lu, X. Wu, X. Wang, H. Li, L. Chen, *Nano Lett.* **2012**, *12*, 2153-2157.

[25] X. Deng, X. Liu, H. Yan, D. Wang, L. Wan, *Sci. China Chem.* **2013**, *57*, 178-183.

[26] J. Zheng, H. Zheng, R. Wang, L. Ben, W. Lu, L. Chen, L. Chen, H. Li, *Phys. Chem. Chem. Phys.* **2014**, *16*, 13229-13238.

[27] V. Kuznetsov, A.-H. Zinn, G. Zampardi, S. Borhani-Haghighi, F. La Mantia, A. Ludwig, W. Schuhmann, E. Ventosa, *ACS Appl. Mater. Interfaces* **2015**, *7*, 23554-23563.

[28] Z. Yang, M. C. Dixon, R. A. Erck, L. Trahey, *ACS Appl. Mater. Interfaces* **2015**, *7*, 26585-26594.

[29] B. Moeremans, H.-W. Cheng, C. Merola, Q. Hu, M. Oezaslan, M. Safari, M. K. Van Bael, A. Hardy, M. Valtiner, F. U. Renner, *Adv. Sci.* **2019**, *6*, 1900190.

[30] I. Yoon, S. Jurng, D. P. Abraham, B. L. Lucht, P. R. Guduru, *Energy Storage Mater.* **2019**, *25*, 296-304.

[31] a) D. Aurbach, M. Daroux, P. Faguy, E. Yeager, *J. Electrochem. Soc.* **1987**, *134*, 1611; b) S.-K. Jeong, M. Inaba, T. Abe, Z. Ogumi, *J. Electrochem. Soc.* **2001**, *148*, A989; c) A. M. Andersson, A. Henningson, H. Siegbahn, U. Jansson, K. Edström, *J. Power Sources* **2003**, *119*, 522-527; d) S. P. Kim, A. C. T. van Duin, V. B. Shenoy, *J. Power Sources* **2011**, *196*, 8590-8597; e) J. Hwang, H. Jang, *J. Electrochem. Soc.* **2014**, *162*, A103-A107; f) Z. Z. Cao, H. W. Meng, P. Dou, C. Wang, J. Zheng, X. H. Xu, *J. Solid State Electrochem.* **2017**, *21*, 955-966; g) Y. Gu, W.-W. Wang, Y.-J. Li, Q.-H. Wu, S. Tang, J.-W. Yan, M.-S. Zheng, D.-Y. Wu, C.-H. Fan, W.-Q. Hu, *Nat. Commun.* **2018**, *9*, 1339; h) I. Yoon, S. Jurng, D. P. Abraham, B. L. Lucht, P. R. Guduru, *Nano Lett.* **2018**, *18*, 5752-5759; i) C. Cao, I. I. Abate, E. Sivonxay, B. Shyam, C. Jia, B. Moritz, T. P. Devereaux, K. A. Persson, H.-G. Steinrück, M. F. Toney, *Joule* **2019**, *3*, 762-781; j) J. Huang, X. Guo, X. Du, X. Lin, J.-Q. Huang, H. Tan, Y. Zhu, B. Zhang, *Energy Environ. Sci.* **2019**, *12*, 1550-1557; k) M. F. He, R. Guo, G. M. Hobold, H. N. Gao, B. M. Gallant, *Proceedings of the National Academy of Sciences* **2020**, *117*, 73-79; l) X. Shen, R. Zhang, X. Chen, X. B. Cheng, X. Li, Q. Zhang, *Adv. Energy Mater.* **2020**, *10*, 1903645.

[32] a) K. Edstrom, M. Herstedt, D. P. Abraham, *J. Power Sources* **2006**, *153*, 380-384; b) C. K. Chan, R. Ruffo, S. S. Hong, Y. Cui, *J. Power Sources* **2009**, *189*, 1132-1140; c) H. Wang, M. Matsui, H. Kuwata, H. Sonoki, Y. Matsuda, X. F. Shang, Y. Takeda, O. Yamamoto, N. Imanishi, *Nat. Commun.* **2017**, *8*, 15106.

[33] a) Y. P. Sun, M. Amirmaleki, Y. Zhao, C. T. Zhao, J. N. Liang, C. H. Wang, K. R. Adair, J. J. Li, T. Cui, G. R. Wang, R. Y. Li, T. Filleter, M. Cai, T. K. Sham, X. L. Sun, *Adv. Energy Mater.* **2020**, *10*, 2001139; b) Y. Zhao, M. Amirmaleki, Q. Sun, C. T. Zhao, A. Codirenzi, L. V. Goncharova, C. H. Wang, K. Adair, X. Li, X. F. Yang, F. P. Zhao, R. Y. Li, T. Filleter, M. Cai, X. L. Sun, *Matter* **2019**, *1*, 1215-1231; c) N.-W. Li, Y. Shi, Y.-X. Yin, X.-X. Zeng, J.-Y. Li, C.-J. Li, L.-J. Wan, R. Wen, Y.-G. Guo, *Angew. Chem. Int. Ed.* **2018**, *57*, 1505-1509.

[34] a) Y. Gao, Z. F. Yan, J. L. Gray, X. He, D. W. Wang, T. H. Chen, Q. Q. Huang, Y. G. C. Li, H. Y. Wang, S. H. Kim, T. E. Mallouk, D. H. Wang, *Nat. Mater.* **2019**, *18*, 384-389; b) M. J. Zachman, Z. Tu, S. Choudhury, L. A. Archer, L. F. Kourkoutis, *Nature* **2018**, *560*, 345-349.

[35] D. Aurbach, Y. Ein-Ely, A. Zaban, *J. Electrochem. Soc.* **1994**, *141*, L1.

[36] A. Lahiri, N. Borisenko, A. Borodin, M. Olschewski, F. Endres, *Phys. Chem. Chem. Phys.* **2016**, *18*, 5630-5637.

[37] a) C. Yan, X. B. Cheng, Y. Tian, X. Chen, X. Q. Zhang, W. J. Li, J. Q. Huang, Q. Zhang, *Adv. Mater.* **2018**, *30*, 1870181; b) G. Yang, S. Frisco, R. M. Tao, N. Philip, T. H. Bennett, C. Stetson, J. G. Zhang, S. D. Han, G. Teeter, S. P. Harvey, Y. Y. Zhang, G. M. Veith, J. Nanda, *ACS Energy Lett.* **2021**, *6*, 1684-1693; c) Y. Zhou, M. Su, X. Yu, Y. Zhang, J.-G. Wang, X. Ren, R. Cao, W. Xu, D. R. Baer, Y. Du, O. Borodin, Y. Wang, X.-L. Wang, K. Xu, Z. Xu, C. Wang, Z. Zhu, *Nat. Nanotechnol.* **2020**, *15*, 224-230.

[38] P. Yu, Q. Sun, Y. Liu, B. Ma, H. Yang, M. Xie, T. Cheng, *ACS Appl. Mater. Interfaces* **2022**, *14*, 7972-7979.

[39] a) J.-F. Ding, R. Xu, X.-X. Ma, Y. Xiao, Y.-X. Yao, C. Yan, J.-Q. Huang, *Angew. Chem. Int. Ed.* **2021**, *134*, e202115602; b) S. Li, Q. Liu, W. Zhang, L. Fan, X. Wang, X. Wang, Z. Shen, X. Zang, Y. Zhao, F. Ma, *Adv. Sci.* **2021**, *8*, 2003240.

[40] Z. Liu, P. Lu, Q. L. Zhang, X. C. Xiao, Y. Qi, L. Q. Chen, *J. Phys. Chem. Lett.* **2018**, *9*, 5508-5514.

[41] K. Guo, R. Kumar, X. Xiao, B. W. Sheldon, H. Gao, *Nano Energy* **2020**, *68*, 104257.

[42] A. von Cresce, S. M. Russell, D. R. Baker, K. J. Gaskell, K. Xu, *Nano Lett.* **2014**, *14*, 1405-1412.

[43] a) P. G. Kitz, M. J. Lacey, P. Novak, E. J. Berg, *Anal. Chem.* **2019**, *91*, 2296-2303; b) Y. G. Chai, W. S. Jia, Z. Q. Hu, S. Jin, H. C. Jin, H. X. Ju, X. B. Yan, H. X. Ji, L. J. Wan, *Chin. Chem. Lett.* **2021**, *32*, 1139-1143; c) T. Liu, L. Lin, X. Bi, L. Tian, K. Yang, J. Liu, M. Li, Z. Chen, J. Lu, K. Amine, K. Xu, F. Pan, *Nat. Nanotechnol.* **2019**, *14*, 50-56.

[44] a) J. B. Goodenough, Y. Kim, *Chem. Mater.* **2010**, *22*, 587-603; b) S. Y. Sun, N. Yao, C. B. Jin, J. Xie, X. Y. Li, M. Y. Zhou, X. Chen, B. Q. Li, X. Q. Zhang, Q. Zhang, *Angew. Chem. Int. Ed.* **2022**, 10.1002/anie.202208743, e202208743.

[45] R. Xu, X. Shen, X. X. Ma, C. Yan, X. Q. Zhang, X. Chen, J. F. Ding, J. Q. Huang, *Angew. Chem. Int. Ed.* **2021**, *60*, 4215-4220.

[46] a) Z. Q. Zhu, Y. X. Tang, Z. S. Lv, J. Q. Wei, Y. Y. Zhang, R. H. Wang, W. Zhang, H. R. Xia, M. Z. Ge, X. D. Chen, *Angew. Chem. Int. Ed.* **2018**, *57*, 3656-3660; b) J. M. Zheng, M. H. Engelhard, D. H. Mei, S. H. Jiao, B. J. Polzin, J. G. Zhang, W. Xu, *Nat. Energy* **2017**, *2*, 8.

[47] G. X. Li, S. P. Liu, Z. Liu, Y. J. Zhao, *Small* **2021**, *17*, 2102196.

[48] J. R. Li, H. Su, M. Li, J. Y. Xiang, X. Z. Wu, S. F. Liu, X. L. Wang, X. H. Xia, C. D. Gu, J. P. Tu, *ACS Appl. Mater. Interfaces* **2021**, *13*, 17690-17698.

[49] H. Qiu, X. Du, J. Zhao, Y. Wang, J. Ju, Z. Chen, Z. Hu, D. Yan, X. Zhou, G. Cui, *Nat. Commun.* **2019**, *10*, 1-12.

[50] W. Deng, X. Wang, *Green Energy Environ.* **2022**, https://doi.org/10.1016/j.gee.2021.12.005.

[51] R. Xu, J. F. Ding, X. X. Ma, C. Yan, Y. X. Yao, J. Q. Huang, *Adv. Mater.* **2021**, *33*, 2105962.

[52] W. Lu, L. Q. Sun, Y. Zhao, T. Wu, L. N. Cong, J. Liu, Y. L. Liu, H. M. Xie, *Energy Storage Mater.* **2021**, *34*, 241-249.

[53] Z. Zhang, S. Guan, S. Liu, B. Hu, C. Xue, X. Wu, K. Wen, C.-W. Nan, L. Li, *Adv. Energy Mater.* **2022**, *12*, 2103332.

[54] S. Liu, X. Ji, N. Piao, J. Chen, N. Eidson, J. Xu, P. Wang, L. Chen, J. Zhang, T. Deng, *Angew. Chem. Int. Ed.* **2021**, *60*, 3661-3671.

[55] a) Y. Liu, D. Lin, P. Y. Yuen, K. Liu, J. Xie, R. H. Dauskardt, Y. Cui, *Adv. Mater.* **2017**, *29*, 1605531; b) Q. Shi, S. Heng, Q. T. Qu, T. Gao, W. J. Liu, L. Hang, H. H. Zheng, *J. Mater. Chem.* **2017**, *5*, 10885-10894; c) S. Jurng, Z. L. Brown, J. Kim, B. L. Lucht, *Energy Environ. Sci.* **2018**, *11*, 2600-2608.

[56] B. Han, X. Li, Q. Wang, Y. Zou, G. Xu, Y. Cheng, Z. Zhang, Y. Zhao, Y. Deng, J. Li, M. Gu, *Adv. Mater.* **2022**, *34*, 2108252.

[57] S. Liu, J. Mao, Q. Zhang, Z. Wang, W. K. Pang, L. Zhang, A. Du, V. Sencadas, W. Zhang, Z. Guo, *Angew. Chem. Int. Ed.* **2020**, *59*, 3638-3644.

[58] W. Xu, H. Wang, J. Hu, H. Zhang, B. Zhang, F. Kang, D. Zhai, *Chem. Commun.* **2021**, *57*, 1034-1037.

[59] N. Xiao, W. D. McCulloch, Y. Wu, *J. Am. Chem. Soc.* **2017**, *139*, 9475-9478.

[60] L. Fan, S. Chen, R. Ma, J. Wang, L. Wang, Q. Zhang, E. Zhang, Z. Liu, B. Lu, *Small* **2018**, *14*, 1801806.

[61] P. Lu, C. Li, E. W. Schneider, S. J. Harris, *J. Phys. Chem. C* **2014**, *118*, 896-903.

[62] C. Chen, Q. Liang, Z. Chen, W. Zhu, Z. Wang, Y. Li, X. Wu, X. Xiong, *Angew. Chem. Int. Ed.* **2021**, *60*, 26718-26724.

[63] a) B. J. Goodno, J. M. Gere, *Mechanics of materials*, Cengage learning, Boston, **2020**; b) W. D. Callister's, *Fundamentals of materials science and engineering*, Wiley, London, **2000**.

[64] a) M. Boniface, L. Quazuguel, J. Danet, D. Guyomard, P. Moreau, P. Bayle-Guillemaud, *Nano Lett.* **2016**, *16*, 7381-7388; b) W. Huang, H. Wang, D. T. Boyle, Y. Li, Y. Cui, *ACS Energy Lett.* **2020**, *5*, 1128-1135.

[65] a) N. Weadock, N. Varongchayakul, J. Wan, S. Lee, J. Seog, L. Hu, *Nano Energy* **2013**, *2*, 713-719; b) H. T. Zhang, D. Y. Wang, C. Shen, *Appl. Surf. Sci.* **2020**, *507*, 145059.

[66] a) W. Huang, P. M. Attia, H. S. Wang, S. E. Renfrew, N. Jin, S. Das, Z. W. Zhang, D. T. Boyle, Y. Z. Li, M. Z. Bazant, B. D. McCloskey, W. C. Chueh, Y. Cui, *Nano Lett.* **2019**, *19*, 5140-5148; b) W.-W. Wang, Y. Gu, J.-H. Wang, Z.-B. Chen, X.-T. Yin, Q.-H. Wu, J.-W. Yan, B.-W. Mao, *J. Electrochem. Soc.* **2022**, *169*, 020563.

[67] D. Aurbach, B. Markovsky, I. Weissman, E. Levi, Y. Ein-Eli, *Electrochim. Acta* **1999**, *45*, 67-86.

[68] S. J. Harris, P. Lu, *J. Phys. Chem. C* **2013**, *117*, 6481-6492.

[69] a) G. Y. Jiang, K. Y. Li, F. Yu, X. L. Li, J. Y. Mao, W. W. Jiang, F. G. Sun, B. Dai, Y. S. Li, *Adv. Energy Mater.* **2021**, *11*, 2003496; b) Z. Y. Lu, W. T. Li, Y. Long, J. C. Liang, Q. H. Liang, S. C. Wu, Y. Tao, Z. Weng, W. Lv, Q. H. Yang, *Adv. Funct. Mater.* **2020**, *30*, 1907343; c) Z. J. Ju, J. W. Nai, Y. Wang, T. F. Liu, J. H. Zheng, H. D. Yuan, O. W. Sheng, C. B. Jin, W. K. Zhang, Z. Jin, H. Tian, Y. J. Liu, X. Y. Tao, *Nat. Commun.* **2020**, *11*, 488; d) D. D. Chen, P. Liu, L. Zhong, S. J. Wang, M. Xiao, D. M. Han, S. Huang, Y. Z. Meng, *Small* **2021**, *17*, e2101496; e) D. D. Chen, S. Huang, L. Zhong, S. J. Wang, M. Xiao, D. M. Han, Y. Z. Meng, *Adv. Funct. Mater.* **2020**, *30*, 1907717; f) S. Y. Li, L. Fan, Y. Y. Lw, *Energy Storage Mater.* **2019**, *18*, 205-212; g) X. Gao, Y. Du, S. Li, J. Zhou, X. Feng, X. Jin, B. Wang, *ACS Appl. Mater. Interfaces* **2019**, *12*, 844-850; h) R. Xu, X. Q. Zhang, X. B. Cheng, H. J. Peng, C. Z. Zhao, C. Yan, J. Q. Huang, *Adv. Funct. Mater.* **2018**, *28*, 1870049; i) G. Song, C. Hwang, W.-J. Song, J.

H. Lee, S. Lee, D.-Y. Han, J. Kim, H. Park, H.-K. Song, S. Park, *Small* **2021**, *18*, 2105724; j) X. R. Li, M. M. Lv, Y. Tian, L. Gao, T. F. Liu, Q. H. Zhou, Y. F. Xu, L. Shen, W. Y. Shi, X. Y. Li, Y. F. Lu, X. Y. Liu, S. X. Xiao, *Nano Energy* **2021**, *87*, 106214; k) T. Chen, H. P. Wu, J. Wan, M. X. Li, Y. C. Zhang, L. Sun, Y. C. Liu, L. L. Chen, R. Wen, C. Wang, *J. Energy Chem.* **2021**, *62*, 172-178; l) M. Wang, L. Huai, G. Hu, S. Yang, F. Ren, S. Wang, Z. Zhang, Z. Chen, Z. Peng, C. Shen, D. Wang, *J. Phys. Chem. C* **2018**, *122*, 9825-9834.

[70] K. Zhao, M. Pharr, L. Hartle, J. J. Vlassak, Z. Suo, *J. Power Sources* **2012**, *218*, 6-14.

[71] L. E. Nielsen, *Mechanical properties of polymers*, Van Nostrand Reinhold, University of Michigan, **1962**.

[72] A. Masias, N. Felten, R. Garcia-Mendez, J. Wolfenstine, J. Sakamoto, *J. Mater. Sci.* **2019**, *54*, 2585-2600.

[73] a) A. Ferrese, P. Albertus, J. Christensen, J. Newman, *J. Electrochem. Soc.* **2012**, *159*, A1615; b) A. Ferrese, J. Newman, *J. Electrochem. Soc.* **2014**, *161*, A1350-A1359.

[74] Y. Liu, K. Guo, C. Wang, H. Gao, *J. Mech. Phys. Solids* **2019**, *123*, 103-118.

[75] Y. He, H. Hu, *Phys. Chem. Chem. Phys.* **2015**, *17*, 23565-23572.

[76] a) M. W. Verbrugge, Y. Qi, D. R. Baker, Y.-T. J. E. E. A. S. F. M. t. P. Cheng, *Electrochemical Engineering Across Scales: From Molecules to Processes* **2015**, 193-225; b) D. P. Karothu, J. Mahmoud Halabi, E. Ahmed, R. Ferreira, P. R. Spackman, M. A. Spackman, P. Naumov, *Angew. Chem. Int. Ed.* **2021**, *134*, e202113988; c) Z. Huang, X. Chen, S. J. O'Neill, G. Wu, D. J. Whitaker, J. Li, J. A. McCune, O. A. Scherman, *Nat. Mater.* **2022**, *21*, 103-109.

[77] N. B. Aetukuri, S. Kitajima, E. Jung, L. E. Thompson, K. Virwani, M.-L. Reich, M. Kunze, M. Schneider, W. Schmidbauer, W. W. Wilcke, D. S. Bethune, J. C. Scott, R. D. Miller, H.-C. Kim, *Adv. Energy Mater.* **2015**, *5*, 1500265.

[78] J. P. Xie, X. D. Li, H. J. Lai, Z. J. Zhao, J. L. Li, W. G. Zhang, W. G. Xie, Y. M. Liu, W. J. Mai, *Angew. Chem. Int. Ed.* **2019**, *58*, 14740-14747.

[79] L. Schafzahl, H. Ehmann, M. Kriechbaum, J. Sattelkow, T. Ganner, H. Plank, M. Wilkening, S. A. Freunberger, *Chem. Mater.* **2018**, *30*, 3338-3345.

[80] M. Tanaka, J. B. Hooper, D. Bedrov, *ACS Appl. Energy Mater.* **2018**, *1*, 1858-1863.

[81] X. Du, Y. Gao, B. Zhang, *Adv. Funct. Mater.* **2021**, *31*, 2102562.

[82] a) X.-R. Liu, X. Deng, R.-R. Liu, H.-J. Yan, Y.-G. Guo, D. Wang, L.-J. Wan, *ACS Appl. Mater. Interfaces* **2014**, *6*, 20317-20323; b) H. Shin, J. Park, S. Han, A. M. Sastry, W. Lu, *J. Power Sources* **2015**, *277*, 169-179; c) S. Q. Huang, L. Z. Cheong, S. W. Wang, D. Y. Wang, C. Shen, *Appl. Surf. Sci.* **2018**, *452*, 67-74; d) C. Shen, G. H. Hu, L. Z. Cheong, S. Q. Huang, J. G. Zhang, D. Y. Wang, *Small Methods* **2018**, *2*, 1700298; e) S. Benning, C. G. Chen, R. A. Eichel, P. H. L. Notten, F. Hausen, *ACS Appl. Energy Mater.* **2019**, *2*, 6761-6767; f) Z. Zhang, K. Smith, R. Jervis, P. R. Shearing, T. S. Miller, D. J. Brett, *ACS Appl. Mater. Interfaces* **2020**, *12*, 35132-35141; g) Z. Cao, X. Y. Zheng, Q. T. Qu, Y. H. Huang, H. H. Zheng, *Adv. Mater.* **2021**, *33*, 2103178; h) Y. Z. Li, J. M. Lu, Z. Y. Wang, X. Y. Wang, H. M. Yuan, N. Qin, Z. B. Yi, Z. H. Chen, S. Gu, Z. G. Lu, *ACS Sustain. Chem. Eng.* **2021**, *9*, 8059-8068; i) S. Y. Yuan, S. T. Weng, F. Wang, X. L. Dong, Y. G. Wang, Z. X. Wang, C. Shen, J. L. Bao, X. F. Wang, Y. Y. Xia, *Nano Energy* **2021**, *83*, 105847; j) H. T. Zhang, C. Shen, Y. B. Huang, Z. P. Liu, *Appl. Surf. Sci.* **2021**, *537*, 147983; k) Y. Li, L. Lv, W. Huang, Y. Zhu, F. Long, W. Zheng, Q. Qu, H. Zheng, *ChemElectroChem* **2021**, *9*, e202101409; l) Y. Qin, K. Xu, Q. Wang, M. Ge, T. Cheng, M. Liu, H. Cheng, Y. Hu, C. Shen, D. Wang, Y. Liu, B. Guo, *Nano Energy* **2022**, *96*, 107082.

[83] a) G. J. Wan, F. H. Guo, H. Li, Y. L. Cao, X. P. Ai, J. F. Qian, Y. X. Li, H. X. Yang, *ACS Appl. Mater. Interfaces* **2018**, *10*, 593-601; b) G. X. Li, Y. Gao, X. He, Q. Q. Huang, S. R. Chen, S. H. Kim, D. H. Wang, *Nat. Commun.* **2017**, *8*, 1-10; c) X. Du, Y. Gao, Z. Hou, X. Guo, Y. Zhu, B. Zhang, *ACS Appl. Energy Mater.* **2022**, *5*, 2252-2259; d) R. Zhou, H. Tan, Y. Gao, Z. Hou,

X. Du, B. Zhang, *Carbon* **2022**, *186*, 141-149; e) J. Zhang, X. Yang, R. Wang, W. Dong, W. Lu, X. Wu, X. Wang, H. Li, L. Chen, *J. Phys. Chem. C* **2014**, *118*, 20756-20762.

[84] C. Cao, S. Mukherjee, J. Liu, B. Wang, M. Amirmaleki, Z. Lu, J. Y. Howe, D. Perovic, X. Sun, C. V. Singh, *Nanoscale* **2017**, *9*, 11678-11684.

[85] a) A. Castellanos-Gomez, M. Poot, G. A. Steele, H. S. Van Der Zant, N. Agraït, G. Rubio-Bollinger, *Adv. Mater.* **2012**, *24*, 772-775; b) S. Timoshenko, S. Woinowsky-Krieger, *Theory of plates and shells, Vol. 2*, McGRAW-HILL New York, **1959**.

[86] J. Vlassak, W. Nix, *J. Mater. Res.* **1992**, *7*, 3242-3249.

[87] S. Cai, D. Breid, A. J. Crosby, Z. Suo, J. W. Hutchinson, *J. Mech. Phys. Solids* **2011**, *59*, 1094-1114.

[88] H. J. Ye, S. W. Gui, Z. F. Wang, J. Z. Chen, Q. N. Liu, X. D. Zhang, P. Jia, Y. S. Tang, T. T. Yang, C. C. Du, L. Geng, H. Li, Q. S. Dai, Y. F. Tang, L. Q. Zhang, H. Yang, J. Y. Huang, *ACS Appl. Mater. Interfaces* **2021**, *13*, 44479-44487.

[89] W. C. Oliver, G. M. Pharr, *J. Mater. Res.* **1992**, *7*, 1564-1583.

[90] a) Y. X. Tang, J. Y. Deng, W. L. Li, O. I. Malyi, Y. Y. Zhang, X. R. Zhou, S. W. Pan, J. Q. Wei, Y. R. Cai, Z. Chen, X. D. Chen, *Adv. Mater.* **2017**, *29*, 1701828; b) A.-H. Zinn, S. Borhani-Haghighi, E. Ventosa, J. Pfetzing-Micklich, N. Wieczorek, W. Schuhmann, A. Ludwig, *Phys. Status Solidi A* **2014**, *211*, 2650-2656; c) Y. Wang, Q. Zhang, D. Li, J. Hu, J. Xu, D. Dang, X. Xiao, Y.-T. Cheng, *Adv. Energy Mater.* **2018**, *8*, 1702578; d) Y. Xu, C. Stetson, K. Wood, E. Sivonxay, C. Jiang, G. Teeter, S. Pylypenko, S.-D. Han, K. A. Persson, A. Burrell, A. Zakutayev, *ACS Appl. Mater. Interfaces* **2018**, *10*, 38558-38564.

[91] a) N. Shpigel, M. D. Levi, S. Sigalov, L. Daikhin, D. Aurbach, *Acc. Chem. Res.* **2018**, *51*, 69-79; b) V. Dargel, N. Shpigel, S. Sigalov, P. Nayak, M. D. Levi, L. Daikhin, D. Aurbach, *Nat. Commun.* **2017**, *8*, 1-8; c) P. G. Kitz, M. J. Lacey, P. Novak, E. J. Berg, *J. Power Sources* **2020**, *477*, 228567.

[92] N. Shpigel, M. D. Levi, D. Aurbach, *Energy Storage Mater.* **2019**, *21*, 399-413.

[93] A. D. Easley, T. Ma, C. I. Eneh, J. Yun, R. M. Thakur, J. L. Lutkenhaus, *J. Polym. Sci.* **2022**, *60*, 1090-1107.

[94] M. V. Voinova, M. Rodahl, M. Jonson, B. Kasemo, *Phys. Scr.* **1999**, *59*, 391.

[95] J. M. Bennett, *Appl. Opt.* **1976**, *15*, 2705-2721.

[96] a) Q. Zhang, X. Xiao, W. Zhou, Y.-T. Cheng, M. W. Verbrugge, *Adv. Energy Mater.* **2015**, *5*, 1401398; b) A. Neubrand, P. Hess, *J. Appl. Phys.* **1992**, *71*, 227-238; c) D. Schneider, in *Handbook of Advanced Nondestructive Evaluation*, Springer international publishing, Switzerland, **2019**, pp. 171-234.

[97] a) Z. Huang, S. Choudhury, N. Paul, J. H. Thienenkamp, P. Lennartz, H. Gong, P. Müller-Buschbaum, G. Brunklaus, R. Gilles, Z. Bao, *Adv. Energy Mater.* **2021**, *12*, 2103187; b) Z. Zhao, J. Zhao, Z. Hu, J. Li, J. Li, Y. Zhang, C. Wang, G. Cui, *Energy Environ. Sci.* **2019**, *12*, 1938-1949.

[98] F. S. Li, Y. S. Wu, J. Chou, M. Winter, N. L. Wu, *Adv. Mater.* **2015**, *27*, 130-137.

[99] S. Park, S. Y. Jeong, T. K. Lee, M. W. Park, H. Y. Lim, J. Sung, J. Cho, S. K. Kwak, S. Y. Hong, N. S. Choi, *Nat. Commun.* **2021**, *12*, 838.

[100] G. Bilodeau, *J. Appl. Mech.* **1992**, *59*, 5190523.

[101] Z. Zhang, Y. Li, R. Xu, W. Zhou, Y. Li, T. Oyakhire Solomon, Y. Wu, J. Xu, H. Wang, Z. Yu, T. Boyle David, W. Huang, Y. Ye, H. Chen, J. Wan, Z. Bao, W. Chiu, Y. Cui, *Science* **2022**, *375*, 66-70.

[102] Y. Gao, S.-Q. Shi, T.-Y. Zhang, *Nanoscale* **2017**, *9*, 6033-6040.

[103] a) X. Du, B. Zhang, *ACS Nano* **2021**, *15*, 16851-16860; b) J. Huang, X. Lin, H. Tan, B. Zhang, *Adv. Energy Mater.* **2018**, *8*, 1703496.

[104] P. T. Xiao, R. P. Luo, Z. H. Piao, C. Li, J. X. Wang, K. Yu, G. M. Zhou, H. M. Cheng, *ACS Energy Lett.* **2021**, *6*, 3170-3179.

[105] R. Seltzer, A. P. Cisilino, P. M. Frontini, Y.-W. Mai, *International Journal of Mechanical Sciences* **2011**, *53*, 471-478.

[106] a) M. J. Wang, K. M. Liechti, J. M. White, R. M. Winter, *J. Mech. Phys. Solids* **2004**, *52*, 2329-2354; b) Y. Kamikawa, K. Amezawa, K. Terada, *J. Phys. Chem. C* **2020**, *124*, 22488-22495.

[107] a) Y. Gao, Y.-J. Sun, T.-Y. Zhang, *Appl. Phys. Lett.* **2016**, *108*, 123104; b) Z. Chen, J. Luo, I. Doudevski, S. Erten, S. H. Kim, *Microsc. Microanal.* **2019**, *25*, 1106-1111.

[108] a) C. A. Clifford, M. P. Seah, *Appl. Surf. Sci.* **2005**, *252*, 1915-1933; b) W. S. LePage, Y. Chen, A. Poli, M. D. Thouless, N. P. Dasgupta, *Extreme Mech. Lett.* **2022**, *52*, 101644.

[109] M. C. Meyers, KA, in *Mechanical Behavior of Materials*, Prentice Hall Upper Saddle River, NJ, **1999**, pp. 98-103.

[110] a) K. Lim, B. Fenk, J. Popovic, J. Maier, *ACS Appl. Mater. Interfaces* **2021**, *13*, 51767-51774; b) J. Popovic, *Energy Technol.* **2021**, *9*, 2001056.

[111] a) F. Allgayer, J. Maibach, F. Jeschull, *ACS Appl. Energy Mater.* **2022**, *5*, 1136-1148; b) H. Bryngelsson, M. Stjerndahl, T. Gustafsson, K. Edstrom, *J. Power Sources* **2007**, *174*, 970-975.

[112] W. Shin, A. Manthiram, *Angew. Chem. Int. Ed.* **2022**, *61*, e202115909.

[113] L. von Kolzenberg, A. Latz, B. Horstmann, *Batter. Supercaps* **2021**, *5*, e202100216.

[114] a) G. M. Veith, M. Doucet, R. L. Sacci, B. Vacaliuc, J. K. Baldwin, J. F. Browning, *Sci. Rep.* **2017**, *7*, 1-15; b) Y. M. Lee, J. Y. Lee, H. T. Shim, J. K. Lee, J. K. Park, *J. Electrochem. Soc.* **2007**, *154*, A515-A519.

[115] A. M. Andersson, K. Edstrom, *J. Electrochem. Soc.* **2001**, *148*, A1100-A1109.

[116] N. S. Choi, K. H. Yew, K. Y. Lee, M. Sung, H. Kim, S. S. Kim, *J. Power Sources* **2006**, *161*, 1254-1259.

[117] T. D. Pham, A. Bin Faheem, K. K. Lee, *Small* **2021**, *17*, 2103375.

[118] S. Mei, S. Guo, B. Xiang, J. Deng, J. Fu, X. Zhang, Y. Zheng, B. Gao, P. K. Chu, K. Huo, *J. Energy Chem.* **2022**, *69*, 616-625.

[119] N. W. Li, Y. X. Yin, C. P. Yang, Y. G. Guo, *Adv. Mater.* **2016**, *28*, 1853-1858.

[120] R. Pathak, K. Chen, A. Gurung, K. M. Reza, B. Bahrami, J. Pokharel, A. Baniya, W. He, F. Wu, Y. Zhou, K. Xu, Q. Qiao, *Nat. Commun.* **2020**, *11*, 93.

[121] a) A. L. Davis, R. Garcia-Mendez, K. N. Wood, E. Kazyak, K. H. Chen, G. Teeter, J. Sakamoto, N. P. Dasgupta, *J. Mater. Chem.* **2020**, *8*, 6291-6302; b) S. T. Oyakhire, W. Huang, H. Wang, D. T. Boyle, J. R. Schneider, C. de Paula, Y. Wu, Y. Cui, S. F. J. A. E. M. Bent, *Adv. Energy Mater.* **2020**, *10*, 2002736; c) Y. Zhao, K. Zheng, X. Sun, *Joule* **2018**, *2*, 2583-2604.

[122] C. Li, Q. Lan, Y. Yang, H. Shao, H. Zhan, *ACS Appl. Mater. Interfaces* **2018**, *11*, 2479-2489.

[123] Q. Wang, J. Wan, X. Cao, R. Wen, Y. Guo, W. Liu, H. Zhou, *Adv. Funct. Mater.* **2021**, *32*, 2107923.

[124] Z. Wang, Y. Wang, Z. Zhang, X. Chen, W. Lie, Y. B. He, Z. Zhou, G. Xia, Z. Guo, *Adv. Funct. Mater.* **2020**, *30*, 2002414.

[125] a) J. W. Suk, S. Murali, J. An, R. S. Ruoff, *Carbon* **2012**, *50*, 2220-2225; b) S. Huang, L. Tang, H. S. Najafabadi, S. Chen, Z. Ren, *Nano Energy* **2017**, *38*, 504-509.

[126] T. Chen, J. Wan, Y. Liu, Z. Jin, H. Wu, W. Feng, R. Wen, C. Wang, *Chem. Eng. J.* **2021**, *433*, 133189.

[127] J. Wan, Y. Hao, Y. Shi, Y.-X. Song, H.-J. Yan, J. Zheng, R. Wen, L.-J. Wan, *Nat. Commun.* **2019**, *10*, 3265.

[128] C. Yan, L. L. Jiang, Y. X. Yao, Y. Lu, J. Q. Huang, Q. Zhang, *Angew. Chem. Int. Ed.* **2021**, *60*, 8521-8525.

[129] W.-W. Wang, Y. Gu, H. Yan, S. Li, J.-W. He, H.-Y. Xu, Q.-H. Wu, J.-W. Yan, B.-W. Mao, *Chem* **2020**, *6*, 2728-2745.

[130] a) D. Aurbach, M. Koltypin, H. Teller, *Langmuir* **2002**, *18*, 9000-9009; b) J. F. Ding, R. Xu, X. X. Ma, Y. Xiao, Y. X. Yao, C. Yan, J. Q. Huang, *Angew. Chem. Int. Ed.* **2022**, *134*, e202115602; c) W.-W. Wang, Y. Gu, H. Yan, K.-X. Li, Z.-B. Chen, Q.-H. Wu, C. Kranz, J.-W. Yan, B.-W. Mao, *Faraday Discuss.* **2022**, *233*, 190-205.

[131] N. Takenaka, H. Sakai, Y. Suzuki, P. Uppula, M. Nagaoka, *J. Phys. Chem. C* **2015**, *119*, 18046-18055.

[132] I. A. Shkrob, J. F. Wishart, D. P. Abraham, *J. Phys. Chem. C* **2015**, *119*, 14954-14964.

[133] Z. Huang, J. Ren, W. Zhang, M. Xie, Y. Li, D. Sun, Y. Shen, Y. Huang, *Adv. Mater.* **2018**, *30*, 1803270.

[134] J. Xie, L. Liao, Y. Gong, Y. Li, F. Shi, A. Pei, J. Sun, R. Zhang, B. Kong, R. Subbaraman, *Sci. Adv.* **2017**, *3*, eaao3170.

[135] C. Ma, X. Zhang, C. Liu, Y. Zhang, Y. Wang, L. Liu, Z. Zhao, B. Wu, D. Mu, *Green Energy Environ.* **2022**, https://doi.org/10.1016/j.gee.2021.12.006.

[136] C. Wu, F. H. Guo, L. Zhuang, X. P. Ai, F. P. Zhong, H. X. Yang, J. F. Qian, *ACS Energy Lett.* **2020**, *5*, 1644-1652.

[137] X. Li, J. M. Zheng, X. D. Ren, M. H. Engelhard, W. G. Zhao, Q. Y. Li, J. G. Zhang, W. Xu, *Adv. Energy Mater.* **2018**, *8*, 10.

[138] a) C. Monroe, J. Newman, *J. Electrochem. Soc.* **2004**, *151*, A880; b) H.-W. Yang, W. S. Kang, S.-J. Kim, *Electrochim. Acta* **2022**, *412*, 140107.

[139] J. Jones, M. Anouti, M. Caillon-Caravanier, P. Willmann, D. Lemordant, *Fluid Phase Equilib.* **2009**, *285*, 62-68.

[140] W. D. Richards, L. J. Miara, Y. Wang, J. C. Kim, G. Ceder, *Chem. Mater.* **2016**, *28*, 266-273.

[141] a) Y. Yu, G. Huang, J. Z. Wang, K. Li, J. L. Ma, X. B. Zhang, *Adv. Mater.* **2020**, *32*, 2004157; b) S. Liu, X. Ji, J. Yue, S. Hou, P. Wang, C. Cui, J. Chen, B. Shao, J. Li, F. Han, J. Tu, C. Wang, *J. Am. Chem. Soc.* **2020**, *142*, 2438-2447.

[142] F. Li, J. He, J. Liu, M. Wu, Y. Hou, H. Wang, S. Qi, Q. Liu, J. Hu, J. Ma, *Angew. Chem. Int. Ed.* **2021**, *60*, 6600-6608.

[143] Y. Liu, X. Tao, Y. Wang, C. Jiang, C. Ma, O. Sheng, G. Lu, X. W. Lou, *Science* **2022**, *375*, 739-745.

[144] H. R. Wang, H. B. Chew, *ACS Appl. Mater. Interfaces* **2017**, *9*, 25662-25667.

[145] S. Dalavi, P. Guduru, B. L. Lucht, *J. Electrochem. Soc.* **2012**, *159*, A642-A646.

[146] a) Z. Liu, Y. Qi, Y. X. Lin, L. Chen, P. Lu, L. Q. Chen, *J. Electrochem. Soc.* **2016**, *163*, A592-A598; b) Y. Y. Wang, Z. J. Wang, L. Zhao, Q. N. Fan, X. H. Zeng, S. L. Liu, W. K. Pang, Y. B. He, Z. P. Guo, *Adv. Mater.* **2021**, *33*, 2008133; c) Y. T. Yan, Y. S. He, X. L. Zhao, W. Y. Zhao, Z. F. Ma, X. W. Yang, *Nano Energy* **2021**, *84*, 105935.

[147] D. Bedrov, O. Borodin, J. B. Hooper, *J. Phys. Chem. C* **2017**, *121*, 16098-16109.

[148] Y. T. Jin, N. J. H. Kneusels, P. Magusin, G. Kim, E. Castillo-Martinez, L. E. Marbella, R. N. Kerber, D. J. Howe, S. Paul, T. Liu, C. P. Grey, *J. Am. Chem. Soc.* **2017**, *139*, 14992-15004.

[149] Y. Kamikawa, K. Amezawa, K. Terada, *J. Phys. Chem. C* **2020**, *124*, 19937-19944.

[150] Z. L. Brown, S. Jurng, C. C. Nguyen, B. L. Lucht, *ACS Appl. Energy Mater.* **2018**, *1*, 3057-3062.

[151] J. H. Cho, X. Xiao, K. Guo, Y. Liu, H. Gao, B. W. Sheldon, *Energy Storage Mater.* **2020**, *24*, 281-290.

[152] D. Aurbach, E. Zinigrad, Y. Cohen, H. Teller, *Solid State Ionics* **2002**, *148*, 405-416.

[153] Y. Jiang, Y. Yang, F. Ling, G. Lu, F. Huang, X. Tao, S. Wu, X. Cheng, F. Liu, D. Li, H. Yang, Y. Yao, P. Shi, Q. Chen, X. Rui, Y. Yu, *Adv. Mater.* **2022**, *34*, 2109439.

[154] Y. Liu, X. Xu, O. O. Kapitanova, P. V. Evdokimov, Z. Song, A. Matic, S. Xiong, *Adv. Energy Mater.* **2022**, *12*, 2103589.

[155] C. Villevieille, *Adv. Mater. Interfaces* **2022**, *9*, 2101865.

[156] H.-S. Lim, W.-J. Kwak, S. Chae, S. Wi, L. Li, J. Hu, J. Tao, C. Wang, W. Xu, J.-G. Zhang, *ACS Energy Lett.* **2021**, *6*, 3321-3331.

[157] a) J. Park, Y. Jeong, M. H. Alfaruqi, Y. Liu, X. Xu, S. Xiong, M.-G. Jung, H.-G. Jung, J. Kim, J.-Y. Hwang, Y.-K. Sun, *ACS Energy Lett.* **2021**, *7*, 401-409; b) X. Wang, M. Chen, S. Li, C. Zhao, W. Zhang, Z. Shen, Y. He, G. Feng, Y. Lu, *ACS Cent. Sci.* **2021**, *7*, 2029-2038.

[158] a) L. Gao, J. Chen, Q. Chen, X. Kong, *Sci. Adv.* **2022**, *8*, eabm4606; b) Z. Yu, H. S. Wang, X. Kong, W. Huang, Y. C. Tsao, D. G. Mackanic, K. C. Wang, X. C. Wang, W. X. Huang, S. Choudhury, Y. Zheng, C. V. Amanchukwu, S. T. Hung, Y. T. Ma, E. G. Lomeli, J. Qin, Y. Cui, Z. N. Bao, *Nat. Energy* **2020**, *5*, 526-533; c) M. A. Hope, B. L. D. Rinkel, A. B. Gunnarsdottir, K. Marker, S. Menkin, S. Paul, I. V. Sergeyev, C. P. Grey, *Nat. Commun.* **2020**, *11*, 2224.

[159] a) M. Schellenberger, R. Golnak, W. Q. Garzon, S. Risse, R. Seidel, *Mater. Today Adv.* **2022**, *14*, 100215; b) Z. Shadike, H. Lee, O. Borodin, X. Cao, X. Fan, X. Wang, R. Lin, S.-M. Bak, S. Ghose, K. Xu, C. Wang, J. Liu, J. Xiao, X.-Q. Yang, E. Hu, *Nat. Nanotechnol.* **2021**, *16*, 549-554.

[160] Z. D. Zeng, N. A. Liu, Q. S. Zeng, S. W. Lee, W. L. Mao, Y. Cui, *Nano Energy* **2016**, *22*, 105-110.

[161] J. Jiao, G. Lai, L. Zhao, J. Lu, Q. Li, X. Xu, Y. Jiang, Y. B. He, C. Ouyang, F. Pan, *Adv. Sci.* **2022**, *9*, 2105574.

[162] a) D. Diddens, W. A. Appiah, Y. Mabrouk, A. Heuer, T. Vegge, A. Bhowmik, *Adv. Mater. Interfaces* **2022**, *9*, 2101734; b) Z. Deng, V. Kumar, F. T. Bölle, F. Caro, A. A. Franco, I. E. Castelli, P. Canepa, Z. W. Seh, *Energy Environ. Sci.* **2022**, *15*, 579-594.

[163] Q. Zhang, J. Ma, L. Mei, J. Liu, Z. Li, J. Li, Z. Zeng, *Matter* **2022**, *5*, 1235-1250.

[164] C. Fang, J. Li, M. Zhang, Y. Zhang, F. Yang, J. Z. Lee, M.-H. Lee, J. Alvarado, M. A. Schroeder, Y. J. N. Yang, *Nature* **2019**, *572*, 511-515.

[165] a) P. Liang, G. Shao, H. Wang, C.-a. Wang, *ACS Appl. Energy Mater.* **2021**, *4*, 3993-4001; b) P. R. Chinnam, L. Xu, L. Cai, N. L. Cordes, S. Kim, C. M. Efaw, D. J. Murray, E. J. Dufek, H. Xu, B. Li, *Adv. Energy Mater.* **2022**, *12*, 2103048.

[166] A. Tokranov, B. W. Sheldon, C. Z. Li, S. Minne, X. C. Xiao, *ACS Appl. Mater. Interfaces* **2014**, *6*, 6672-6686.

[167] H. Bulter, F. Peters, G. Wittstock, *Energy Technol.* **2016**, *4*, 1486-1494.

[168] a) B. L. Mehdi, J. Qian, E. Nasybulin, C. Park, D. A. Welch, R. Faller, H. Mehta, W. A. Henderson, W. Xu, C. M. Wang, J. E. Evans, J. Liu, J. G. Zhang, K. T. Mueller, N. D. Browning,

Nano Lett. **2015**, *15*, 2168-2173; b) J. Xiong, N. Dupré, P. Moreau, B. Lestriez, *Adv. Energy Mater.* **2022**, *12*, 2103348.

[169] A. Kushima, K. P. So, C. Su, P. Bai, N. Kuriyama, T. Maebashi, Y. Fujiwara, M. Z. Bazant, J. Li, *Nano Energy* **2017**, *32*, 271-279.

[170] L. Han, T. F. Liu, O. W. Sheng, Y. J. Liu, Y. Wang, J. W. Nai, L. Zhang, X. Y. Tao, *ACS Appl. Mater. Interfaces* **2021**, *13*, 45139-45148.

[171] M. Chouchane, O. Arcelus, A. A. Franco, *Batter. Supercaps* **2021**, *4*, 1457-1463.

[172] a) M. Kim, Z. Z. Yang, I. Bloom, *J. Electrochem. Soc.* **2021**, *168*, 9; b) I. Andriunas, Z. Milojevic, N. Wade, P. K. Das, *J. Power Sources* **2022**, *525*, 231126; c) D. Li, G. Zhu, H. Liu, Y. Wang, *Micromachines* **2022**, *13*, 142; d) A. J. Louli, M. Genovese, R. Weber, S. G. Hames, E. R. Logan, J. R. Dahn, *J. Electrochem. Soc.* **2019**, *166*, A1291-A1299.

[173] X. Hu, Y. Gao, B. Zhang, L. Shi, Q. Li, *EcoMat* **2022**, 10.1002/eom2.12264, e12264.

[174] a) J. X. Zheng, M. S. Kim, Z. Y. Tu, S. Choudhury, T. Tang, L. A. Archer, *Chem. Soc. Rev.* **2020**, *49*, 2701-2750; b) D. Lin, Y. Liu, Y. Cui, *Nat. Nanotechnol.* **2017**, *12*, 194-206; c) S. Li, M. Jiang, Y. Xie, H. Xu, J. Jia, J. Li, *Adv. Mater.* **2018**, *30*, 1706375; d) B. Liu, J. G. Zhang, W. Xu, *Joule* **2018**, *2*, 833-845; e) A. Naveed, A. Ali, T. Rasheed, X. Wang, P. Ye, X. Li, Y. Zhou, S. Mingru, Y. Liu, *J. Power Sources* **2022**, *525*, 231122.

[175] a) D. Kang, M. Xiao, J. P. Lemmon, *Batter. Supercaps* **2021**, *4*, 445-455; b) X. Liang, Q. Pang, I. R. Kochetkov, M. S. Sempere, H. Huang, X. Sun, L. F. Nazar, *Nat. Energy* **2017**, *2*, 17119.